

# Oscillatory flow around a vertical circular cylinder placed in an open channel: coherent structures, sediment entrainment potential and drag forces

Wen-Yi Chang<sup>1</sup> and George Constantinescu<sup>2,†</sup>

<sup>1</sup>National Center for High-Performance Computing, National Applied Research Laboratories, Hsinchu 30076, Taiwan

<sup>2</sup>Department of Civil and Environmental Engineering & IIHR Hydroscience and Engineering, The University of Iowa, Iowa City IA 52242, USA

(Received 7 July 2022; revised 12 December 2022; accepted 25 April 2023)

Flow and turbulent structures generated by the interaction of forced incoming oscillatory flow with a circular, vertical cylinder placed in an open channel with a horizontal bed are investigated using eddy-resolving simulations. Validation simulations performed with a Keulegan–Carpenter ( $KC$ ) number of 20 and multiple-mode forcing corresponding to the laboratory experiment of Sumer *et al.* (*J. Fluid Mech.*, vol. 332, 1997, pp. 41–70) show that detached eddy simulation (DES) predicts more accurately the amplification of the bed shear stress beneath the horseshoe vortex system (upstream side of the cylinder) and the maximum magnitude of the bed shear stress at the downstream (wake) side of the cylinder compared with unsteady Reynolds-averaged Navier–Stokes simulations. High-Reynolds-number DES simulations are then conducted with  $1.5 \leq KC \leq 30.8$  and one-mode sinusoidal forcing of the streamwise velocity in the approaching flow to investigate the changes in the wake vortex-flow regimes, the coherence of the horseshoe vortices and the generation of other near-bed coherent structures in the wake during the oscillatory cycle. The flow is periodic, no horseshoe vortices form and no vortices are shed in the wake for  $KC = 1.5$ . By contrast, for  $KC \geq 8$  horseshoe vortices are present over part of the oscillatory cycle and up to three wake vortices are shed over each half-cycle as  $KC$  is increased to 30.8. For an intermediate range of  $KC$  numbers, one ( $KC = 15.4$ ) or two ( $KC = 8$ ) of the vortices forming at the back of the cylinder during each half-cycle are washed around it when the flow reverses. The main horseshoe vortex and other horizontal near-bed vortices have a large capacity to amplify the bed shear stresses when the incoming velocity magnitude is significantly less than its peak value.

† Email address for correspondence: [sconstan@engineering.uiowa.edu](mailto:sconstan@engineering.uiowa.edu)

Assuming the depth-averaged velocity in the incoming (undisturbed) oscillatory flow is the same in simulations conducted with different  $KC$  numbers, the peak values of the sediment entrainment potential measured by the mean (cycle-averaged) volumetric flux of sediment entrained from the bed over one oscillatory cycle occur for  $8 \leq KC \leq 15.4$ . For all  $KC$  numbers, the in-line force variation over the oscillatory cycle is fairly well approximated by the Morison equation. For  $KC = 1.5$ , the in-line force is only due to inertia effects. For  $KC = 30.8$ , the maximum and minimum values of the phase-averaged in-line force are approximately in phase with those of the incoming flow velocity. For  $KC \geq 15$ , the phase-averaged in-line force coefficients vary between 0.8 and 1.1 during most of the oscillatory cycle (e.g. when the incoming flow velocity is not close to zero). This is different from cases with  $KC \leq 8$  where the in-line force coefficient is equal to zero twice during the oscillatory cycle as the in-line force becomes equal to zero for non-zero values of the incoming velocity. The largest cycle-to-cycle variations of the in-line force coefficient and in-line force are observed around  $KC = 8$ . For  $KC = 8$  and 15.4, the cylinder is subject to relatively large phase-averaged spanwise drag forces that are comparable to the peak phase-averaged streamwise drag forces. As  $KC$  is increased to 30.8, the phase-averaged spanwise drag force becomes zero over the whole oscillatory cycle but the cylinder is still subject to large instantaneous spanwise forces over part of the oscillatory cycle.

**Key words:** coastal engineering, vortex dynamics, vortex shedding

---

## 1. Introduction

Deeper understanding of the physics of oscillatory flow past a solid vertical cylinder mounted on a channel bed is useful for several engineering applications. Such a flow serves as a canonical test case for understanding sediment erosion mechanisms and the relationship between the unsteady forcing of the approaching flow and the capacity of the flow to induce sediment entrainment and local scour around piles placed in marine environments. As such, a main application is related to safe design of monopile foundations of offshore structures (e.g. wind turbines). Of particular concern is the local scour that can erode the seabed around the base of a foundation due to the action of waves and/or tidal currents. Depending on the flow conditions in the field, scour holes with maximum depths of several metres can develop over a short period around offshore foundation structures. Use of a rock-armour apron around the base of the pile is by far the most common scour protection measure for this type of structure (Louwersheimer, Verhagen & Olthof 2009; Petersen *et al.* 2014). Designing the apron in terms of its size and the mean diameter of the rock to be used requires accurate information on the maximum bed shear stress and the positions of the regions of high bed shear induced by the unsteady flow before scour begins (e.g. for flat-bed conditions around a monopile). Knowledge of the unsteady forces acting on the submerged part of the structure is essential for both strength and fatigue design of offshore wind turbines. Other applications include understanding transport processes and ecological implications for isolated emerged plant stems in shallow coastal waters, understanding heat transfer for heat exchangers in marine environments and quantifying fatigue damage by wave-induced loads for the columns of semi-submersible platforms in marine environments (Kamsanam 2014; Liu *et al.* 2016; Zang, Tang & Nepf 2017). In such applications, the approaching flow generally has a strong oscillatory component due to waves or other unsteady flow conditions in the marine environment.

The case of a surface-mounted, emerged, circular solid cylinder in steady incoming flow with flat and deformed (e.g. scoured) bed has been the object of detailed experimental and numerical studies focusing on the dynamics of the large-scale coherent structures (e.g. see Dargahi 1989; Sumer & Fredsøe 1997; Akili & Rockwell 2002; Roulund *et al.* 2005; Kirkil & Constantinescu 2009, 2012, 2015; Apsilidis *et al.* 2015; Baykal *et al.* 2015, 2017). These studies have shown that at conditions corresponding to the start of the bed scouring process (e.g. flat-bed conditions), scour is driven by the flow acceleration around the sides of the cylinder and by the horseshoe vortex system forming around the upstream base of the cylinder. Though the coherence of the horseshoe vortices is highly variable in time, the main horseshoe vortex is always present in the flow fields if the degree of bluntness of the cylinder is sufficiently high. The large erosion potential of the horseshoe vortex system even for flat-bed conditions was explained by the fact that the main horseshoe vortex is subject to large-scale bimodal oscillations (Simpson 2001; Kirkil & Constantinescu 2015). The core of the vortex undergoes sweeping, low-frequency motions towards and away from the upstream face of the cylinder. As a result, the size of the region where high bed shear stresses and sediment entrainment are induced at different times in the instantaneous flow fields is much larger compared with that expected for a relatively stable main horseshoe vortex that is subject only to small oscillations around its mean-flow position.

The same studies showed that the presence of the channel bed had a noticeable influence on the billow vortices shed in the wake. While for flat-bed conditions, the anti-symmetric vortex-shedding mode was present (similar to the von Kármán vortex street for long cylinders), the cores of the wake vortices were vertical only close to the free surface. Near the bed, the cores of the wake vortices were stretched and became inclined with respect to the vertical, which decreased their overall capacity to induce large bed shear stresses. Another important effect was observed at high Reynolds numbers where the attached boundary layers on the circular cylinder were turbulent before separation (supercritical Reynolds numbers) and the flow separated at polar angles larger than  $100^\circ$ . Close to the bed, where the approaching velocity is small due to the bottom boundary layer, the flow separated at about  $90^\circ$  and the vortex shedding resembled that observed for long cylinders at subcritical Reynolds numbers. Wake vortices generated for subcritical flow conditions have a much-reduced capacity to induce large bed shear stresses compared with vortices generated for cases where the separation line is vertical until the bed (e.g. for rectangular and square cylinders, see discussion in Kirkil & Constantinescu 2009) and to entrain particles from the channel bed. Finally, the presence of the channel bed also induced strong three-dimensional (3-D) effects at the back of the cylinder where a pair of streamwise-oriented, counter-rotating vortices formed. These vortices were shown to play an important role in the weakening of the anti-symmetric mode especially once the scour hole starts developing (Kirkil, Constantinescu & Ettema 2009).

The structure of oscillatory flow around a surface-mounted cylinder and the dynamics of the large-scale coherent eddies were less investigated. The dynamics of both the wake flow on the downstream (lee) side of the cylinder and of the horseshoe vortices forming around the upstream face of the cylinder is much more complex compared with the case of an incoming steady current (Sumer, Christiansen & Fredsøe 1997; Baykal *et al.* 2017). Similar to the simpler case of oscillatory flow around a long cylinder parallel to the free surface or of an oscillating long cylinder in steady flow (e.g. see Keulegan & Carpenter 1958; Sarpkaya & Issacson 1981; Williamson 1985; Obasaju, Bearman & Graham 1988), the Keulegan–Carpenter number,  $KC = U_m T/D$  ( $T$  is the period of the oscillatory flow,  $U_m$  is the maximum depth-averaged streamwise velocity at large distances from the cylinder,  $D$  is the cylinder diameter), is the main parameter that determines the structure of the wake

flow and the number of vortices shed over each half-cycle (Sumer *et al.* 1997). As opposed to the case of an incoming steady current, horseshoe vortices are present only over part of the oscillatory cycle and only for sufficiently high  $KC$  numbers. In the case where the cylinder is placed on a loose bed, the wake vortices may have a larger capacity to entrain particulates and induce local scour compared with the horseshoe vortices (Sumer *et al.* 1997).

Given the importance of protecting foundations of wind turbines and bridge piers against excessive local scour in marine environments, the focus of most of the previous experimental and numerical investigations was on predicting the scour evolution and the equilibrium scour bathymetry around surface-mounted vertical piles and investigating the efficiency of different scour protection measures (e.g. rock armour). Some investigations focused on predicting the decrease of the scour hole as a result of reducing the amplitude of the waves approaching the pile, a process called backfilling (Sumer *et al.* 2003). Three-dimensional Reynolds-averaged Navier Stokes (RANS) investigations were quite successful in predicting the temporal evolution of the scour hole at foundations of offshore structures starting either with an initially flat bed or with a scoured bed in the case of backfilling (Stahlmann 2014; Baykal *et al.* 2017). However, no numerical study based on large-eddy simulation (LES) techniques that can accurately capture the unsteady dynamics of the energetically important coherent structures in the flow was conducted for surface-mounted vertical cylinders in oscillatory flow. For example, unsteady RANS (URANS)-based models cannot capture the aperiodic oscillations of the main horseshoe vortices forming around the upstream face of a cylinder placed in a steady current. Though URANS was shown to correctly capture the dependence between the number of wake vortices shed at the back of a cylinder in oscillatory flow and the  $KC$  number (Baykal *et al.* 2017), some discrepancies between the RANS predictions of the bed shear stresses and the experimental data were present. In general, RANS accuracy is less than that of LES, or similar eddy-resolving techniques, in terms of predicting the mean-flow quantities in complex turbulent flows. Moreover, there is much evidence that RANS is less accurate than LES in terms of capturing the dynamics of the vortex tubes in the separated shear layers, the coherence of the shed vortices and the complex interactions among coherent structures generated around a surface-mounted bluff body (e.g. see Kirkil & Constantinescu 2009; Keylock, Constantinescu & Hardy 2012). So, LES-based techniques are better suited to investigate the flow physics and the role of large-scale turbulence in such flows.

Away from the channel bottom, the oscillatory wake flow past a surface-mounted cylinder is very similar to the oscillatory wake flow past a long, isolated cylinder at similar  $KC$  and Reynolds ( $Re = U_m D / \nu$ , where  $\nu$  is the molecular viscosity) numbers. Most oscillatory-flow experimental studies were conducted at low Reynolds numbers that are far from those encountered in most applications related to marine structures. For example, Tatsuno & Bearman (1990) discussed the two-dimensional (2-D) and 3-D flow regimes observed for a circular cylinder oscillating in a tank of water for  $KC \leq 12$ ,  $Re < 1200$  and Stokes numbers  $\beta = Re/KC < 100$ . The same is true for numerical studies conducted using 2-D and 3-D direct numerical simulations (e.g. see Justensen 1991; Dutsch *et al.* 1998; Nehari & Ballio 2004; Elston, Blackburn & Sheridan 2006; Zhao & Cheng 2014; Tong *et al.* 2017). Generally, 2-D numerical simulations successfully predict the 2-D vortex-shedding patterns and the forces acting on the cylinder for relatively low Reynolds and Stokes numbers. The experimental study of Williamson (1985) provided detailed information on the wake structure in planes perpendicular to the axis of the cylinder for flow past an oscillating cylinder in a tank of water for a much wider range of  $KC$  and Stokes numbers ( $KC \leq 40$  and  $\beta < 730$ ). His experiments revealed an increase

$KC = TU_m/D$	$D/H$	$Re_a = aU_m/\nu$	$TU_m/H$	$\tau_m/\rho U_m^2$
1.5	0.325	31 050	0.5	0.0043
8.0	0.325	165 600	2.6	0.00295
15.4	0.325	318 800	5	0.0027
30.8	0.325	637 600	10	0.0024

Table 1. Main non-dimensional flow and geometrical variables for the test cases conducted with purely oscillatory flow (one-mode forcing).

of the number of shed vortices over each oscillatory cycle with increasing  $KC$  number (e.g. from no vortices shed for  $KC < 7$  to four pairs of vortices shed for  $KC > 32$ ). A transverse shedding regime was also observed at intermediate  $KC$  numbers ( $7 < KC < 15$ ). For sufficiently large  $KC$  numbers, the anti-symmetric vortex shedding generates vortices whose subsequent dynamics may induce significant lift or spanwise forces on the cylinder (e.g. some of the vortices generated on one side of the cylinder may be advected to the other side over the next half of the oscillatory cycle) and a quasi-periodic, multiple-mode variation of the drag and lift forces even for cases with one mode (e.g. sinusoidal) forcing in the incoming, unidirectional oscillatory flow. Three-dimensional effects may be important even at relatively low Reynolds and Stokes numbers (e.g. see Tatsuno & Bearman 1990; Yang & Rockwell 2002). As for the case of steady incoming flow past a cylinder, 3-D effects are expected to become stronger at much higher Reynolds numbers than those considered in the aforementioned laboratory-scale investigations.

The present study investigates the effects of the  $KC$  number on flow and turbulence structure generated by a circular cylinder of diameter  $D$  placed in open channel of depth  $H$  in unidirectional, purely oscillatory flow using detached eddy simulation (DES). The channel bed is horizontal and smooth. Comparison with results of URANS simulations is also included. Following validation with the experimental data of Sumer *et al.* (1997) conducted for a case with multiple-mode forcing of the incoming streamwise velocity,  $D/H = 0.5$ ,  $Re \approx 7200$  and  $KC \approx 20$  corresponding to experimental Test 14, a series of high-Reynolds-number simulations are conducted with  $1.5 \leq KC \leq 30.8$ ,  $D/H = 0.325$ ,  $Re \approx 130\,000$  and one-mode sinusoidal forcing (table 1). The Reynolds number is large enough for the wake to be strongly turbulent.

Given that a major goal of the present paper is to investigate the physics of oscillatory flow past cylinders at sufficiently high Reynolds numbers (e.g.  $Re > 10^5$ ) where the turbulence structure is fairly similar that one observed in field studies, the main options are the use of classical LES with wall functions or of a hybrid RANS–LES approach. Given the success of DES in simulating high-Reynolds-number separated flows past bluff bodies (Spalart 2009; Koken & Constantinescu 2011; Rodi, Constantinescu & Stoesser 2013), the latter approach is used. Away from the walls, the eddy viscosity predicted by DES is proportional to the square of the local grid spacing and the rate of strain magnitude, like in a classical Smagorinsky model. As a result, DES behaves as LES with a more sophisticated near-wall model. Using a one- or two-equation RANS model to solve the flow inside the viscous sublayer and next to it avoids the use of wall functions and the associated assumption that the law-of-the-wall is valid near solid surfaces, which is the main reason why LES with wall functions is not very accurate in complex flows with strong adverse pressure gradients and massive separation, like the flows investigated in this study. For flows past surface-mounted cylinders, DES was shown to accurately capture not only the

wake structure but also the complex dynamics (e.g. bimodal oscillations) of the horseshoe vortices forming around the upstream face of the cylinder (Kirkil & Constantinescu 2015).

A first goal of the paper is to describe the wake vortex–flow regimes in the presence of a no-slip bottom boundary for relatively shallow conditions ( $D/H < 1$ ) and the dynamics of the horseshoe vortices and of the other near-bed coherent structures generated during the oscillatory cycles over a fairly large range of  $KC$  numbers. A second goal is to describe the dominant sediment entrainment mechanisms based on the instantaneous and phase-averaged bed shear stress distributions around the cylinder. Of particular interest is to describe how the coherent structures forming in the vicinity of the channel bed affect sediment entrainment and transport and to point to similarities to and differences from erosion processes observed in the well-studied case of steady incoming flow past a vertical cylinder placed in a channel. One important research question is what is the variation of the sediment entrainment capacity of the flow with increasing  $KC$  number? A related question is what is the contribution of the coherent structures whose dynamics is not quasi-periodic and of the smaller-scale turbulence to the sediment entrainment capacity of the oscillatory flow? A third goal is to determine the phase-averaged forces acting on the cylinder during the oscillatory cycle and their standard deviation as a function of the  $KC$  number. One related question is how do the magnitudes of the instantaneous and phase-averaged spanwise drag forces compare with those of the streamwise drag forces for different  $KC$  numbers?

Section 2 briefly discusses the numerical method, the boundary conditions and the main flow and geometrical parameters of the test cases. Section 3 compares the DES and URANS predictions of bed shear stresses with those from an experiment performed by Sumer *et al.* (1997) for flow around a vertical cylinder exposed to waves ( $KC = 20$ ). Section 4 focuses on the effect of the  $KC$  number on the bed shear stress distributions for oscillatory flow past a vertical cylinder with one-mode sinusoidal forcing. The same section analyses the wake-vortex-shedding regimes, the horseshoe vortex flow dynamics and the other flow features and large-scale turbulent structures playing an important role in the amplification of the bed shear stresses. Section 5 analyses the effect of the  $KC$  number on the volumetric flux of entrained sediment per unit time over the oscillatory cycle and the average capacity of the oscillatory flow to entrain sediment over the full cycle. Section 6 discusses how the  $KC$  number affects the variations of the phase-averaged forces acting on the cylinder, the phase-averaged in-line force coefficient and their standard deviations over the oscillatory cycle. The same section discusses the use of Morison's equation to provide predictions of the phase-averaged in-line force over the oscillatory cycle. Section 7 summarizes the main findings and presents some conclusions.

## 2. Numerical model, boundary conditions and test cases

Detached eddy simulation is a hybrid model that combines LES away from the solid boundaries with RANS close to solid boundaries to account for the unresolved turbulence (Spalart 2009). In the shear stress transport (SST) version of DES (Strelets 2001), transport equations are solved for the turbulent kinetic energy,  $k$ , and the turbulence specific dissipation rate,  $\omega$ . For smooth surfaces, the turbulence length scale used in the computation of the dissipation rate in the transport equation for  $k$  is redefined as  $d_{DES} = C_{DES}\Delta$ , where  $\Delta = \min(\Delta x, \Delta y, \Delta z)$ . The model constant is  $C_{DES} = 0.61$ . The SST version of DES is less sensitive to grid resolution restrictions compared with the classical Spalart–Allmaras version of DES (Strelets 2001; Spalart 2009).

At Reynolds numbers at which the boundary layers on the cylinders are laminar at separation, the performance of DES in predicting mean flow and turbulence statistics for

flow past long (circular) cylinders was shown to be comparable with that of well-resolved LES and superior to URANS (Travin *et al.* 2000; Spalart 2009). Detached eddy simulation was successfully used to predict flow past surface-mounted circular and rectangular cylinders and arrays of surface-mounted cylinders (e.g. see Kirkil & Constantinescu 2009, 2015; Chang *et al.* 2011, 2013; Chang, Constantinescu & Tsai 2017, 2020; Zeng & Constantinescu 2017; Koken & Constantinescu 2020). These studies have shown that for steady incoming flow conditions, DES can accurately predict the wake structure and dynamics of the shed billow vortices, the dynamics of the main horseshoe vortices and their interactions with the vortex tubes shed in the separated shear layers. In particular, Kirkil & Constantinescu (2009) compared results of well-resolved LES conducted using the dynamic Smagorinsky model and a fully non-dissipative code with DES for flow past a surface-mounted circular cylinder with  $D/H \approx 1$  and a cylinder Reynolds number of 18 000. The agreement between the two simulations in terms of the predicted mean velocity, turbulent kinetic energy and total turbulence production term was found to be very satisfactory both inside the near-wake region and inside the horseshoe vortex system. Detached eddy simulation successfully captured the bimodal oscillations of the main horseshoe vortex.

To generate a unidirectional oscillatory flow, an unsteady forcing term,  $f_x$ , is added to the streamwise momentum equation. With this modification, the Navier–Stokes equations are

$$\frac{\partial u_i}{\partial x_i} = 0, \quad (2.1)$$

$$\frac{\partial u_i}{\partial t} + \frac{\partial(u_i u_k)}{\partial x_k} = -\frac{\partial p}{\partial x_i} - \frac{\partial}{\partial x_k} \left[ (v + \nu_t) \left( \frac{\partial u_i}{\partial x_k} + \frac{\partial u_k}{\partial x_i} \right) \right] + f_x \delta_{i1}, \quad (2.2)$$

where  $u_i$  is the instantaneous velocity component along the  $i$  direction,  $x_i$  is the  $i$  coordinate ( $x_1 = x$ ,  $x_2 = y$ ,  $x_3 = z$ ),  $\nu_t$  is the eddy/subgrid-scale viscosity,  $p$  is the instantaneous pressure,  $\delta_{ij}$  is the Kronecker symbol and  $i = 1$  corresponds to the streamwise direction in which the forcing is applied. The eddy/subgrid-scale viscosity is obtained either from a RANS model or from DES. The governing equations for the  $k$ – $\omega$  SST model used to perform the URANS simulations can be found in Wilcox (2006). The delayed version of DES, which preserves the RANS mode inside the attached boundary layers, was used (Spalart 2009). The governing equations for delayed DES are given in Rodi *et al.* (2013).

A finite-volume method is used to integrate the discretized incompressible Navier–Stokes equations and the turbulence model equations over each control volume in a time-accurate way. The Gauss divergence theorem is used to convert volume integrals to surface integrals. A collocated grid layout is used such that the control volumes are identical for all transport equations. The convective terms in the momentum equations are discretized using a blend of second-order-accurate upwind biased scheme and second-order central scheme. A procedure similar to the classical algorithm of Rhie & Chow (1983) is used to estimate the advecting velocity at each integrating point in which a higher-order pressure redistribution term, which scales with the mesh spacing, is added (Mahesh, Constantinescu & Moin 2004). The second-order backward upwind scheme is used for time integration. A fully implicit discretization of the governing equations is used at each time step. Multiple inner iterations are performed at each time step. A coupled solver with algebraic multigrid and lower–upper factorization technique is used to solve the discrete system of linearized equations. In the simulations discussed in the present

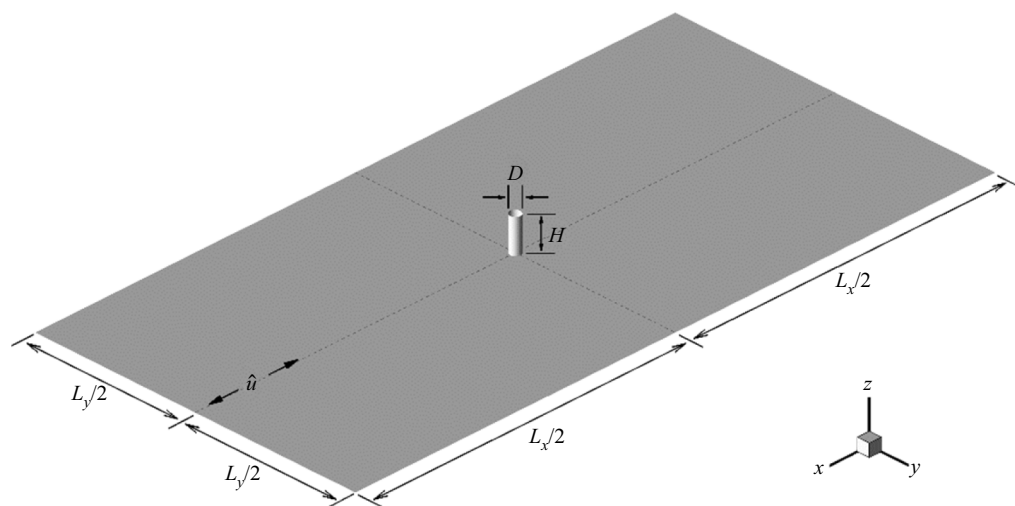


Figure 1. Sketch of the computational domain with the main physical dimensions. Series of simulations were conducted with  $D/H = 0.5$ ,  $L_x/H = 15$ ,  $L_y/H = 7.5$  and with  $D/H = 0.325$ ,  $L_x/H = 20$ ,  $L_y/H = 10$ . The depth-averaged velocity in the oscillatory flow at large distances from the cylinder is  $\hat{u}$ .

study the mesh was fine enough to resolve the near-wall flow (e.g. viscous sublayer) and no wall functions were used.

The computational domain used in the numerical simulations is shown in figure 1. The channel bed is located at  $z = 0$  and the top boundary at  $z = H$  ( $z' = z/H = 1$ ). The origin of the system of coordinates is located at the centre of the solid cylinder. The streamwise direction is  $x$ , while the spanwise direction is  $y$ . The streamwise and spanwise lengths of the computational domain are  $L_x$  and  $L_y$ , respectively. Periodic boundary conditions are applied in the streamwise direction. Slip-wall boundary conditions are imposed at the two lateral boundaries for the velocity components and turbulence variables. No-slip boundary conditions are imposed on the channel bottom and on the cylinder's surface. The turbulent kinetic energy is set to zero, while  $\omega$  is calculated using the standard formula for smooth walls used with the low-Reynolds-number version of the  $k-\omega$  model (Zeng, Constantinescu & Weber 2008). Similar to the oscillatory flow simulations of Baykal *et al.* (2017) and to most studies investigating flow past surface-mounted cylinders placed in open channels with steady incoming flow (e.g. Kirkil & Constantinescu 2015), the top boundary is modelled as a shear-free slip wall. A zero surface-normal gradient is specified for the flow and turbulence variables. As opposed to the experiments of Sumer *et al.* (1997), the present simulations are conducted with no waves at the free surface. Rather it is the imposed forcing along the  $x$  direction that drives the oscillatory flow. Simulations were run with a non-dimensional time step of  $0.001TU_m/H$ . This low value allowed resolving the range of energetic frequencies associated with the dynamically important coherent structures in the flow. After the initial transients were eliminated, phase-averaged quantities were collected over a time interval of 20 cycles ( $\Delta t = 20T$ ). The mesh contained around 5 million cells and 55 points were used to resolve the flow in the vertical direction. The mesh was refined near the cylinder and close to the bed surface.

The first set of simulations were performed mostly for validation purposes. The geometrical and flow conditions were close to those of Test 14 ( $D = 0.04$  m,  $H = 0.08$  m,  $U_m = 0.183$  m s<sup>-1</sup>) in the experimental study of Sumer *et al.* (1997) conducted in a wave



flume with a plane bed. The main non-dimensional parameters were  $D/H = 0.5$ ,  $KC = 20$  and  $Re = 7200$ . A multimodal forcing was applied in the DES and URANS simulations to try to mimic as close as possible the experimentally measured oscillatory streamwise velocity away from the cylinder (undisturbed flow). After several trials, the final expression for the non-dimensional forcing was  $f'_x = f_x(H/U_m^2) = (0.626 \cos(2\pi t/T) + 0.312 \cos(4\pi t/T) + 0.158 \cos(6\pi t/T))$ . For both DES and URANS, the non-dimensional, depth-averaged streamwise velocity at large distances away from the cylinder was  $\hat{u}' = \hat{u}/U_m = 0.95 \sin(2\pi t/T) + 0.26 \sin(4\pi t/T) + 0.08 \sin(6\pi t/T)$ . Its peak values are close to 1 and  $-1$ . Similar to the experiment, an asymmetry is present between the wave crest and the wave trough in the streamwise velocity signal over a cycle. The DES and URANS simulations were performed in a domain with  $L_x/H = 15$  and  $L_y/H = 7.5$ . The first grid point was placed at around 0.15 wall units from the channel bed and at about 1.5 wall units from the surface of the cylinder, where the non-dimensional distance in wall units,  $n^+$ , corresponding to the physical distance to a smooth wall surface,  $n$ , is calculated as  $n^+ = (n/H)(u_\tau/U_m)Re$  assuming conservatively that the non-dimensional bed shear velocity is  $u_\tau/U_m = 0.06$ .

A second set of mostly DES were performed to study the changes in the flow physics and oscillatory behaviour of relevant flow variables with increasing  $KC$  number ( $1.5 \leq KC \leq 30.8$ ). All simulations (table 1) were conducted with  $D/H = 0.325$  and  $Re \approx 130\,000$  in a domain with  $L_x/H = 20$  and  $L_y/H = 10$ . A non-dimensional unimodal forcing  $f'_x = a_x \cos(2\pi t/T)$  was applied such that the streamwise velocity in the undisturbed flow is  $\hat{u}' = \hat{u}/U_m = \sin(2\pi t/T)$  for all cases. The values of the Reynolds number,  $Re_a$ , defined with the semi-excursion length,  $a = U_m T/2\pi$ , are also included in table 1. The physical significance of the variable  $a$  is the amplitude of the undisturbed oscillatory flow in a deep oscillatory boundary layer over a smooth wall. The peak  $|\hat{u}|$  values are reached at  $t = T/4$  and  $t = 3T/4$  and  $\hat{u}$  changes signs at  $t = T/2$ . Given the anti-symmetric oscillatory pattern, the phase-averaged flow can be studied only over half of the period of the oscillatory cycle. For each of the four test cases, the non-dimensional amplitude of the applied forcing  $a_x/(U_m\omega) = 1$ , where  $\omega = 2\pi/T$  is the angular frequency. Formally, one can consider that simulations were performed with constant values of  $D$ ,  $H$  and  $U_m$  and varying periods of the oscillatory cycle,  $T$ . Given that the first grid point off each solid surface is situated within the viscous sublayer, the shear stresses on the solid surfaces are calculated using the definition rather than using the law of the wall. The maximum phase-averaged bed shear stress recorded during the oscillatory cycle in the undisturbed flow is denoted  $\tau_m$ . Its non-dimensional values are also included in table 1.

The RANS simulations and DES were performed using the same meshes. The simulations were run on 64 processors of a PC cluster. The RANS solutions became periodical or quasi-periodical after about 2 weeks. Another 2–3 weeks of physical time were needed to calculate the phase-averaged flow. The DES was run starting from RANS after the RANS solution became quasi-periodical. About 3 weeks of simulation time was needed for the flow to become quasi-periodic in DES. Another 5–7 weeks were needed to calculate the quasi-periodic flow over 20 shedding cycles. This corresponds to about 100 000 CPU hours per DES. A LES with wall functions at the same Reynolds number will reduce the computational time by only about 20 %–30 %.

### 3. Validation simulations

At large distances from the cylinder, the values of the phase-averaged streamwise velocity,  $\bar{u}$ , predicted by DES and URANS are close to identical over the whole

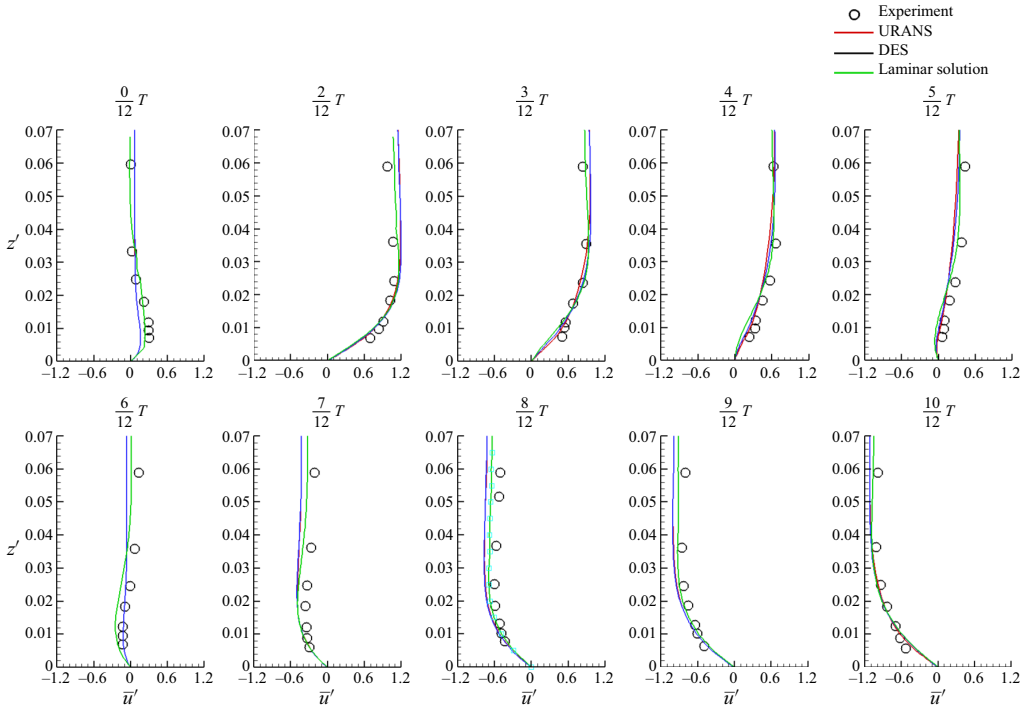


Figure 2. Phase-averaged streamwise velocity profiles,  $\bar{u}'(z/H) = \bar{u}/U_m$ , during the oscillatory cycle ( $0 \leq t \leq 10T/12$ ) predicted by URANS and DES in the symmetry plane ( $y/H=0$ ) at  $x/H=-7.5$ . The non-dimensional vertical distance is  $z' = z/H$ . The symbols show the velocity profiles measured by Sumer *et al.* (1997) for oscillatory flow with no cylinder present in the flume. The green line shows the theoretical solution for an oscillatory laminar boundary layer based on the imposed oscillatory flow containing three modes.

oscillatory cycle. This can be observed from figure 2 that compares the vertical profiles of the non-dimensional phase-averaged streamwise velocity,  $\bar{u}' = \bar{u}/U_m$ , predicted by the numerical simulations in the symmetry plane ( $y/H=0$ ) at  $x/H=-7.5$  with the experimental measurements of Sumer *et al.* (1997) for an oscillatory flow ( $Re = 7200$ ,  $Re_a = 11\,465$ ) with no cylinder present in the flume and with the theoretical laminar solution for an oscillatory boundary layer corresponding to the three-mode forcing. The wave boundary layer was essentially laminar for this test case. The slight disagreement between the predicted profiles and those obtained from the superposition of theoretical solutions corresponding to each mode is mainly due to the small effect induced by the cylinder at the locations of the inlet and outlet sections in the numerical simulations. Given the multimodal forcing, the velocity profiles at  $t=t_0$  and  $t=t_0 + T/2$  are not anti-symmetric. The numerical simulations accurately capture the temporal evolution of  $\bar{u}'$  over the oscillatory cycle outside of the bottom boundary layer where  $\bar{u}'$  does not vary with the distance from the bed. Some small errors are observed over the second half of the oscillatory cycle ( $0.5T < t < T$ ). The velocity variation inside the bottom boundary layer at different times during the oscillatory cycle is also fairly well reproduced by the numerical simulations (figure 2).

Consistent with the corresponding experimental observations of Sumer *et al.* (1997), a horseshoe vortex is observed over about 65%–70% of each oscillatory half-cycle in which the incoming flow is oriented towards one side of the cylinder. Figure 3 compares

## Oscillatory flow around a vertical circular cylinder

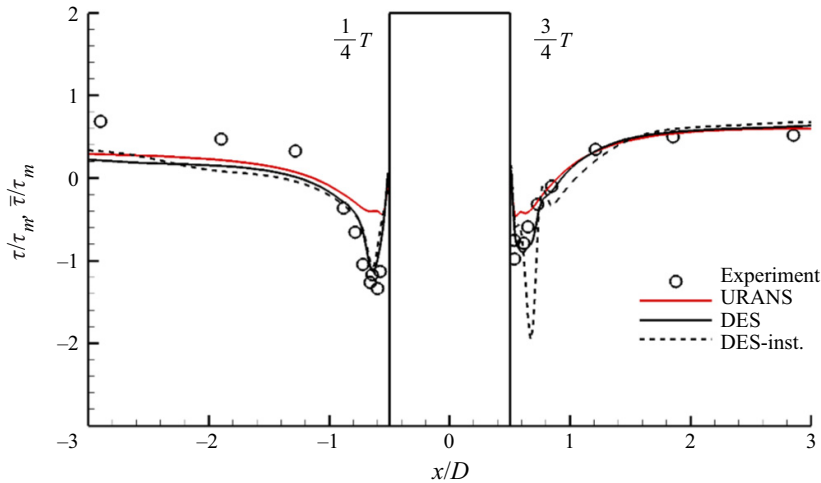


Figure 3. Non-dimensional bed shear stress,  $\tau/\tau_m$  and  $\bar{\tau}/\tau_m$ , inside the symmetry plane ( $y/H=0$ ) at the upstream (horseshoe vortex) side of the cylinder at  $t=T/4$  and  $t=3T/4$  during the oscillatory cycle. Solid lines represent phase-averaged values. The dashed line shows  $\tau/\tau_m$  (DES) during one of the oscillatory cycles when the presence of the horseshoe vortices results in a large amplification of the bed shear stresses close to one side of the cylinder. The symbols show the experimental data (phase-averaged values) of Sumer *et al.* (1997) for  $KC = 20$  (Test 14).

the numerical predictions of the non-dimensional, phase-averaged bed shear stress,  $\bar{\tau}/\tau_m$ , inside the symmetry plane ( $y/H=0$ ) at two time instances ( $t=T/4$  and  $t=3T/4$ ) when the magnitude of the depth-averaged streamwise velocity in the undisturbed flow is relatively high (e.g.  $|\hat{u}'|$  is close to 1) and a strongly coherent horseshoe vortex is present near the upstream base of the cylinder. At both time instances, the bed shear stresses are shown only on the side containing the horseshoe vortex. The presence of a coherent horseshoe vortex induces an amplification of the bed shear stress near the upstream face of the cylinder relative to the incoming flow direction. The peak values of  $\bar{\tau}/\tau_m$  predicted by the present URANS simulations are close to  $-0.55$  at  $t=T/4$  and  $t=3T/4$ , in very good agreement with the peak values predicted by the  $k-\omega$  URANS simulations of Baykal *et al.* (2017). The RANS simulations strongly underestimate the peak values measured by Sumer *et al.* (1997) which are close to  $-1.4$  at  $t=T/4$  and  $-1$  at  $t=3T/4$ . By contrast, DES predictions of  $\bar{\tau}/\tau_m$  in the  $y/H=0$  plane are much closer to the experimental measurements. In particular, the peak values of  $\bar{\tau}/\tau_m$  are about  $-1.2$  at  $t=T/4$  and  $-0.87$  at  $t=3T/4$ . Consistent with the experiment and the asymmetric variation of the incoming flow velocity over the oscillatory cycle, DES predicts a larger magnitude of the peak value of  $\bar{\tau}/\tau_m$  at  $t=T/4$  compared with  $t=3T/4$ .

It is also relevant to point out that Sumer *et al.* (1997) mentioned that over some of the cycles the peak instantaneous values of  $\tau/\tau_m$  can be as high as two times the phase-averaged values. This is also the case in the present DES. Figure 3 also includes the variation of  $\tau/\tau_m$  over one of the cycles where the coherence and circulation of the main horseshoe vortex forming during the trough half-period are very large. For this oscillatory cycle, the peak values of  $\tau/\tau_m$  are close to  $-2$  at  $t=3T/4$ . A similar behaviour is also observed over the crest half-period for some of the oscillatory cycles. Though significant cycle-to-cycle variations are also observed in the instantaneous distributions of  $\tau/\tau_m$  in the RANS simulation, the relative difference between the peak instantaneous value and

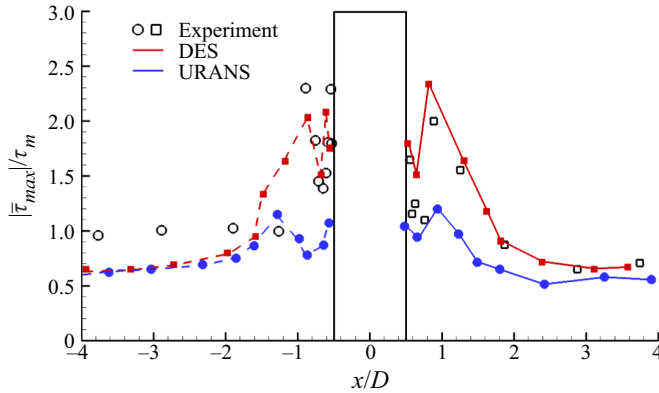


Figure 4. Maximum, phase-averaged bed shear stress magnitude,  $|\bar{\tau}_{max}|/\tau_m$ , in the  $y/H=0$  plane at the downstream (wake) side of the cylinder. The solid lines and square symbols show the peak values recorded over the first half (crest half-period) of the oscillatory cycle  $0 < t < T/2$  ( $u' > 0$ ) for  $x/D > 0.5$ . The dashed lines and the circle symbols show the peak values recorded over the second half (trough half-period) of the oscillatory cycle  $T/2 < t < T$  ( $u' < 0$ ) over the region  $x/D < -0.5$ . The symbols show the experimental data of Sumer *et al.* (1997) for  $KC = 20$  (Test 14).

the peak phase-averaged value is of the order of only 25 %. Both DES and RANS predict that the incoming boundary layer separates in the  $y/H=0$  plane at  $|x_s|/D = 0.8\text{--}0.85$  ( $\bar{\tau}/\tau_m = 0$ ,  $x_s$  is measured from the face of the cylinder) at both  $t = T/4$  and  $t = 3T/4$ , in good agreement with the value ( $|x_s|/D \approx 0.9$ ) measured by Sumer *et al.* (1997). Overall, these results show that DES can capture more accurately the variation in the coherence of the horseshoe vortices forming over part of the oscillatory cycles.

Both RANS and DES predict the shedding of two vortices over each half-cycle, which is consistent with observations from the corresponding ( $KC = 20$ ) experiment of Sumer *et al.* (1997), the experiments conducted with isolated long cylinders by Williamson (1985) and several numerical studies (An, Cheng & Zhao 2015; Baykal *et al.* 2017). Experimental data suggest that for a fairly large range of  $KC$  numbers, the wake vortices forming in oscillatory flow past a surface-mounted cylinder have a larger capacity to entrain sediment than the horseshoe vortices. This is also the case for the present test case ( $KC = 20$ ) for which the measured maximum phase-averaged bed shear stress magnitude  $|\bar{\tau}_{max}|/\tau_m$  in the  $y/D=0$  plane is close to 2.3 over the crest half-period of the oscillatory cycle and 2.0 over the trough half-period (figure 4). These values are larger than those measured beneath the horseshoe vortex system ( $|\bar{\tau}_{max}|/\tau_m \approx 1.4$ ). Similar to the trends observed for the upstream (horseshoe vortex) side of the cylinder, DES predictions of the peak bed shear stress magnitudes on the downstream (lee-wake) side of the cylinder ( $|\bar{\tau}_{max}|/\tau_m \approx 2.2$  over the crest half-period and  $|\bar{\tau}_{max}|/\tau_m = 2.35$  over the trough half-period) are fairly close to the experimental values. Meanwhile, RANS severely underpredicts these values for both half-periods of the oscillatory cycle ( $|\bar{\tau}_{max}|/\tau_m \approx 1$ ). The  $k\text{--}\omega$  RANS of Baykal *et al.* (2017) predicted  $|\bar{\tau}_{max}|/\tau_m \approx 1.3$ . Moreover, DES predictions of the decay of  $|\bar{\tau}_{max}|/\tau_m$  away from the cylinder are in very good agreement with the experiment over the trough half-period.

The largest amplification of the phase-averaged bed shear stress around the cylinder occurs near the sides of the cylinder in the region of strong flow acceleration forming when the velocity magnitude of the incoming flow is close to its peak values. Inside this region, DES predicts  $|\bar{\tau}_{max}|/\tau_m \approx 3.8$  while the experimental measurements of Sumer *et al.* (1997) indicate  $|\bar{\tau}_{max}|/\tau_m \approx 3.5$ .

#### 4. Effect of the $KC$ number on wake vortex shedding, bed shear stress and horseshoe vortex system

##### 4.1. Wake structure during the oscillatory cycle

Figure 5 visualizes the vortical structure around the cylinder using the  $Q$  criterion (Dubief & Delcayre 2000). The quantity  $Q = -0.5\partial u_i/\partial x_j \times \partial u_j/\partial x_i (H^2/U_m^2)$  is the second invariant of the resolved velocity gradient tensor. For all simulations conducted with  $KC \geq 8$ , vortices are shed in the wake. Though the cores of these wake vortices are subject to large-scale deformations along their axes, these vortices remain close to vertical from the top surface to the bed surface. This is different from the case of a surface-mounted circular cylinder with steady incoming flow where the cores of the wake vortices tilt as they approach the bed mostly because of the stretching induced inside the bottom boundary layer. This finding is consistent with the observations of Baykal *et al.* (2017) based on URANS simulations. Present results show that the amplitude of the along-the-axis deformations of the cores of the wake vortices decreases with decreasing  $KC$ . The distance from the cylinder at which the wake vortices remain coherent increases with increasing  $KC$  number. For  $KC = 30.8$  these vortices remain coherent until about  $6D$  from the centre of the cylinder. This distance reduces to about  $3D$  for  $KC = 8$ .

One important finding is that for all the cases where wake shedding is present, the near-bed wake region contains a number of horizontal secondary vortices parallel to the bed (see HSV vortices forming on the downstream side of the cylinder in figure 5). These vortices play a similar role to the horseshoe vortices (HV vortices in figure 5) forming around the upstream side of the cylinder in terms of locally enhancing the instantaneous bed shear stresses. The HSV vortices generally form in between the cores of the (vertical) wake vortices (e.g. such vortices are observed at  $t = T/4$  in figure 5a and at  $t = T/4$  and  $3T/8$  in figure 5b), but some of them can penetrate on the outer side of the region containing the wake vortices (e.g. this is the case at  $t = 3T/8$  in figure 5a). For lower  $KC$  numbers where the wake shedding near the cylinder becomes more symmetric, the HSV vortices generally form close to the symmetry plane (see figure 5c for  $KC = 8$ ). Additionally, a weaker HSV vortex can form around the downstream face of the cylinder, similar to the much more coherent horseshoe vortex present around its upstream face (figure 5c). The HSV vortices are generated mainly because of the interactions among the shed wake vortices and the presence of the no-slip bed surface. Similar to the streamwise-oriented secondary ‘finger’ vortices forming in the wake of a long cylinder (Mahesh *et al.* 2004), the formation of the near-bed horizontal vortices in figure 5 is favoured by the large-scale instabilities generated along the (vertical) cores of the wake vortices. Capturing the dynamics of these secondary vortices requires a LES-based approach.

The main effect of increasing the  $KC$  number is to generate an increasing number of wake vortices on the downstream (lee) side of the cylinder over each half-period of the oscillatory cycle. The wake vortex shedding is in the anti-symmetric mode in all test cases with  $KC \geq 15.4$  (e.g. see instantaneous vertical vorticity plots in figure 6 for  $KC = 30.8$ ). The wake vortex shedding over the oscillatory cycles is fairly regular, which explains the close-to-symmetric patterns of the phase-averaged vorticity,  $\overline{\omega_z}$ , in figure 6. By  $t = T/4$  when the incoming velocity peaks, two counter-rotating vortices have been shed in the wake and another one is detaching from the cylinder (see  $\omega_z$  panel in figure 6a). This explains why two pairs of positive/negative vorticity patches are observed in the distribution of  $\overline{\omega_z}H/U_m$  in figure 6(a). By  $t = 3T/8$  (figure 6b), three counter-rotating vortices are shed in the wake, with a fourth vortex being attached to the cylinder. The fourth vortex remains attached to the cylinder until the incoming flow changes direction

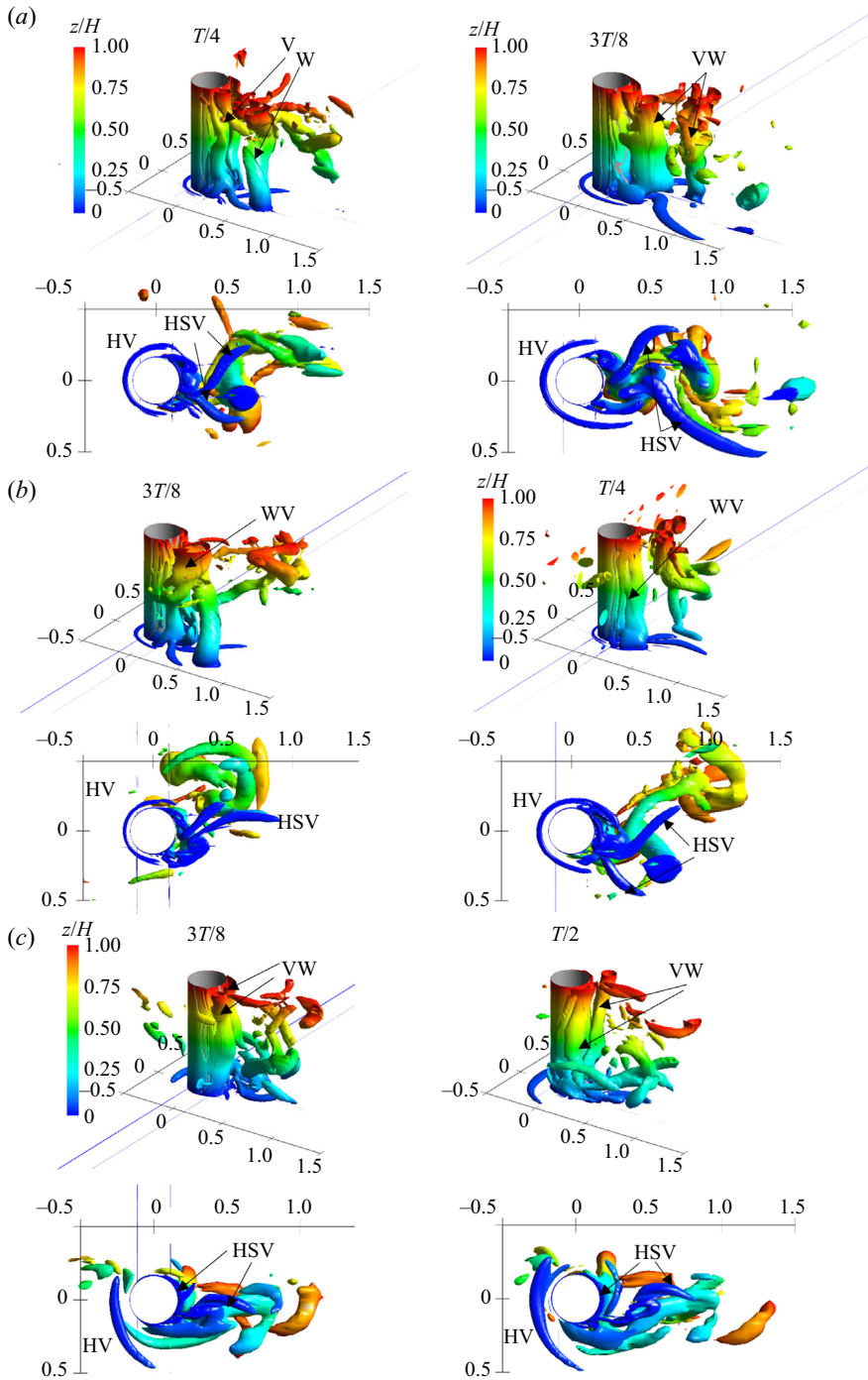


Figure 5. Visualization of the coherent structures in the instantaneous flow fields (DES predictions): (a)  $KC = 30.8$ ; (b)  $KC = 15.4$ ; (c)  $KC = 8$ . The  $Q$  isosurface ( $Q = 10.0$ ) is coloured with the distance from the channel bottom,  $z' = z/H$ . Besides the 3-D view, a vertical view from below the channel bed is included to better visualize the near-bed (dark blue) vortices that are parallel to the channel bottom. To facilitate discussion of the effect of vortical structures on the bed shear stress distributions (view from above the channel bed in figures 8 and 9), the vertical views are rotated by  $180^\circ$  around the  $x$  axis. The horseshoe vortices, horizontal near-bed secondary vortices and main vertical wake vortices are denoted HV, HSV and WV, respectively.

## Oscillatory flow around a vertical circular cylinder

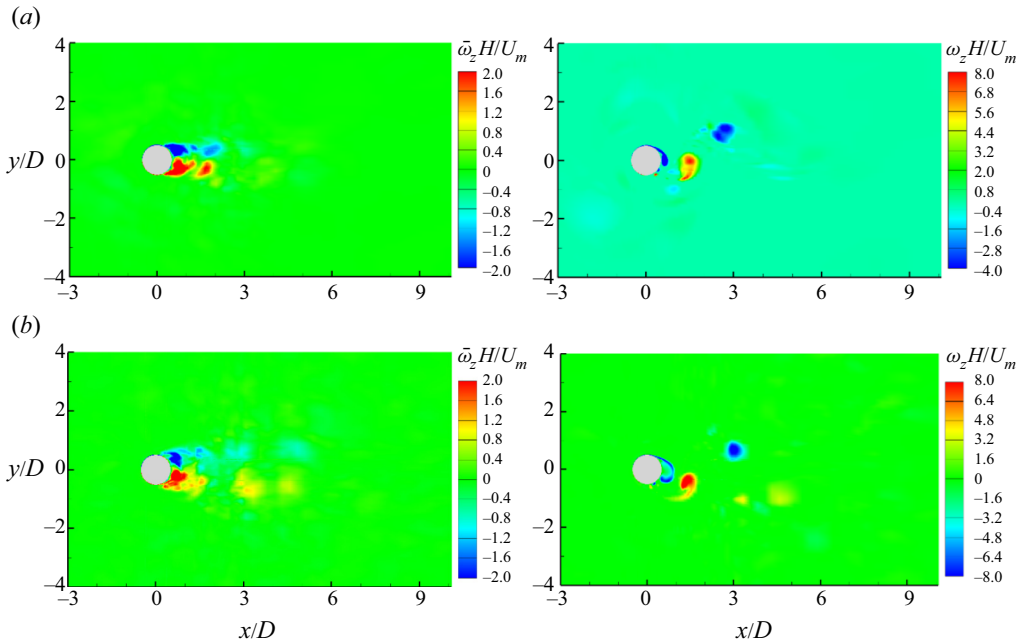


Figure 6. Non-dimensional phase-averaged and instantaneous vertical vorticity,  $\overline{\omega}_z H/U_m$  and  $\omega_z H/U_m$ , during the oscillatory cycle in the  $z/H=0.5$  plane for the  $KC=30.8$  test case (DES predictions): (a)  $t=T/4$  ( $\hat{u}'=1$ ); (b)  $t=3T/8$  ( $\hat{u}'=0.7$ ).

at  $t=T/2$ . The interactions and trajectories of the wake vortices are very irregular as the flow decelerates and the incoming flow velocity approaches zero. The  $KC=30.8$  case is characterized by the formation of four wake vortices and the shedding of three of these vortices every half-cycle. This shedding pattern for  $KC=30.8$  is somewhat expected given that Sumer *et al.* (1997) also observed an increase of the number of shed vortices with increasing  $KC$  with two vortices being shed each half-cycle for  $17 < KC < 23$ .

The anti-symmetric mode weakens considerably as the  $KC$  number decreases towards the threshold value at which vortices are shed in the wake. This can be observed in the  $KC=8$  case where the two counter-rotating vortices forming at the back of the cylinder are fairly symmetric (e.g. see figures 5c and 7b). None of these vortices moves in the wake of the cylinder between  $t=0$  and  $t=T/2$ . As the incoming flow reverses ( $t > T/2$ ), these two vortices are advected along the lateral sides of the cylinder and move into the new wake region. This is also why the mean vorticity distributions in figure 7(a) ( $t=T/4$ ) contain two pairs of counter-rotating vortices. The pair situated around  $x/D=1.5$  does not correspond to vortices shed in the wake between  $t=0$  and  $t=T/4$  but to vortices forming at the back of the cylinder in the  $x/D < 0$  region between  $t=-T/2$  and  $t=0$  that moved into the  $x/D > 0$  region over the next half-period. Consistent with this dynamics, the vorticity sign is different inside the vortices forming on the two sides of the symmetry plane ( $y/D=0$ ) at  $t=T/4$  (figure 7a). This is different from what is observed in cases where the shed vortices remain on the side of the cylinder where they originated (e.g. see  $\overline{\omega}_z$  distributions in figure 6a,b).

Figures 5(c) and 7(b) visualize the two close-to-symmetric vortices forming at the back of the cylinder ( $x/D > 0$ ) in the  $KC=8$  case at two times ( $t=3T/8$  and  $t=T/2$ ) when their coherence is close to maximum. As these two vortices start moving towards and past

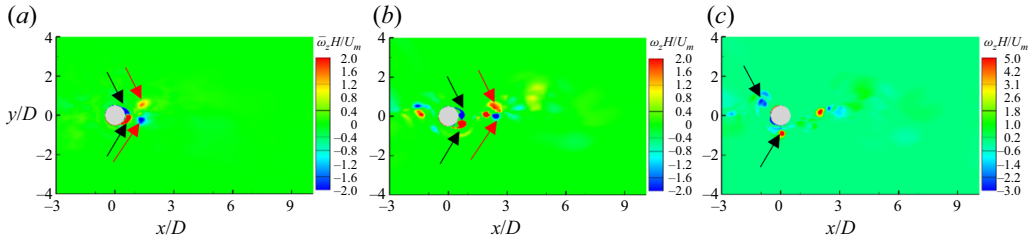


Figure 7. Non-dimensional vertical vorticity, during the oscillatory cycle in the  $z/H = 0.5$  plane for the  $KC = 8$  test case (DES predictions): (a)  $\bar{\omega}_z H/U_m$  at  $t = T/4$  ( $\hat{u}' = 1$ ); (b)  $\omega_z H/U_m$  at  $t = 3T/8$  ( $\hat{u}' = 0.7$ ); (c)  $\omega_z H/U_m$  at  $t = 5T/8$  ( $\hat{u}' = -0.7$ ). The black arrows show the positions of the two vortices forming at the back of the cylinder ( $x/D > 0$ ) for  $0 < t < T/2$ . These two vortices move in the  $x/D < 0$  region over the next half-cycle ( $T/2 < t < T$ ). The red arrows point to the two vortices that formed in the  $x/D < 0$  region for  $-T/2 < t < 0$  and were advected in the  $x/D > 0$  region over the next half-cycle.

the cylinder for  $t > T/2$ , one vortex becomes more coherent than the other (e.g. higher circulation) and their advection speeds become different. Moreover, their trajectories are no longer symmetric with respect to the  $y/D = 0$  plane. This can be observed in the  $\omega_z H/U_m$  distribution at  $t = 5T/8$  (figure 7c) where the (red) wake vortex being advected in the  $y/D < 0$  region is situated at  $x/D \approx 0$  while the (blue) wake vortex being advected in the  $y/D > 0$  region is situated at  $x/D \approx -0.9$ .

The wake shedding in the  $KC = 15.4$  case presents some important similarities to and differences from those discussed for the  $KC = 30.8$  and  $KC = 8$  cases. For brevity, figures are not included to illustrate the wake dynamics for this case. In the  $KC = 15.4$  case, only one vortex is shed in the wake of the cylinder over each half of the oscillatory cycle. This vortex can be seen on the right-hand side of the cylinder in figure 5(b) at  $t = T/4$  and  $3T/8$ . Thus, the wake shedding is anti-symmetric. Lowering the  $KC$  number from 30.8 to 15.4 decreases the number of shed vortices over each half of the oscillatory cycle from three to one. However, rather than remaining on the side of the cylinder where it originated, the vortex shed in the  $KC = 15.4$  case will start moving back towards the cylinder and then past it as the incoming flow changes direction during the next half-cycle. This is similar to what was observed in the  $KC = 8$  case except that only one vortex is washed out around the cylinder each half-cycle, a result also consistent with the experiments of Sumer *et al.* (1997). The vortex moving past the cylinder in the  $KC = 15.4$  case strongly interacts with the vortex forming on the other side of the cylinder over the next half-cycle. Finally, the degree of cycle-to-cycle variability of the wake shedding is the largest in the  $KC = 15.4$  case. This is because for some oscillatory cycles a second weaker vortex of opposite-sign circulation to the first wake vortex is shed during one of the half-cycles.

#### 4.2. Bed shear stress distributions

Besides the vortices shed from the cylinder and the horizontal near-bed vortices, the other vortices with a significant capacity to induce sediment entrainment are the horseshoe vortices forming around the upstream face of the cylinder. The mechanism for the formation of horseshoe vortices in oscillatory flow is the same as that for a surface-mounted cylinder with steady incoming flow. The main difference is that horseshoe vortices form on both sides of the cylinder during each oscillatory cycle as the flow accelerates towards the upstream face of the cylinder. The coherence of these vortices starts decaying and their cores move away from the bed as the flow decelerates. As for the case of cylinders with steady incoming flow, the coherence of the main horseshoe vortex



in the instantaneous flow fields varies with the polar angle. Simulation results in [figure 5](#) show that the degree of asymmetry of the necklace vortex with respect to the symmetry plane is quite high for  $KC \geq 8$ . For example, the legs of the horseshoe vortex are generally not oriented along the streamwise direction, one leg extends further downstream compared with the other leg and/or the size of its core is generally highly asymmetric with respect to the symmetry plane (e.g. see [figure 5c](#) for  $KC = 8$ ). This behaviour is mostly due to the much stronger interactions between the cores of the shed wake vortices, which remain vertical as the bed is approached, and the legs of the main horseshoe vortex compared with the interactions observed for cases with steady incoming flow.

Both the horseshoe vortices and the lower parts of the wake vortices interact with the bed surface. The passage of these eddies and/or variations in their position and coherence over time have a great effect on the amplification of the instantaneous bed shear stresses around the cylinder. In particular, the passage of wake vortices can induce lots of sediment entrainment at locations where the mean (phase-averaged) value of the bed friction velocity magnitude is smaller than the critical threshold value for entrainment given by the Shields diagram or other methods used to estimate this variable for sediment with a given mean particle diameter,  $d_{50}$  (Cheng, Koken & Constantinescu 2018). Therefore, in [figure 8](#) we analyse both the distributions of  $|\bar{\tau}|/\tau_m$  and  $|\tau|/\tau_m$ .

For  $KC = 30.8$ , the maximum values of  $|\bar{\tau}|/\tau_m$  are recorded when the incoming flow velocity magnitude peaks at  $t = T/4$  and  $5T/4$ . Similar to what is observed for cylinders mounted on a horizontal surface with an incoming steady current (Kirkil & Constantinescu 2015), the two main regions of high bed shear stress in [figure 8\(a\)](#) are situated between polar angles of  $30^\circ$  and  $60^\circ$  measured from the symmetry plane ( $y/D = 0$ ). The peak values of  $|\bar{\tau}|/\tau_m$  inside these regions are close to 5. These values are slightly larger than those reported by Sumer *et al.* (1997) for cases when the incoming oscillatory flow was multimodal. Due to the anti-symmetric vortex shedding, the sizes of these regions are generally not equal in the instantaneous flow fields ([figure 8a](#)). Moreover, instantaneous bed shear stresses of comparable magnitude can be induced beneath the wake vortex that detaches from the back of the cylinder (see [figures 5a](#) and [8a](#) for  $t = T/4$ ). In the case of steady incoming flow, such wake vortices with a high sediment entrainment potential are generally observed for cylinders with sharp edges that favour the formation of vortices whose cores remain vertical until the bed surface is reached (Kirkil & Constantinescu 2009). Here, the cross-section of the cylinder does not contain any corner, but the oscillatory flow favours the formation of wake vortices whose axes remain vertical (see discussion of [figure 5](#)). This explains the much larger capacity of these vortices to entrain sediment when the incoming flow past the circular cylinder is oscillatory rather than steady.

Interestingly, as the flow starts decelerating, the region of high bed shear stress around the upstream face of the cylinder is situated beneath the main horseshoe vortex. This means that the horseshoe vortex rather than the flow ‘acceleration’ induced by the presence of the cylinder controls sediment entrainment over part of the oscillatory cycle. As opposed to the case of cylinders with incoming steady current, a region of high mean (phase-averaged) bed shear stress is also forming near the back of the cylinder as the flow is decelerating (e.g. for  $0.5 < x/D < 2$  in [figure 8b](#)). Moreover, additional regions of high instantaneous bed shear stress ( $|\tau|/\tau_m > 2$ ) are present in the wake at  $t = T/4$  ([figure 8a](#)) and  $t = 3T/8$  ([figure 8b](#)). As already discussed, some of these patches of high  $|\tau|/\tau_m$  correspond to the cores of the shed vortices. However, the elongated patches making a low angle with the streamwise direction are induced by the near-bed horizontal vortices forming in the wake (see HSV vortices in [figure 5a](#) for  $t = T/4$  and  $t = 3T/8$ ). As expected, the mean bed shear

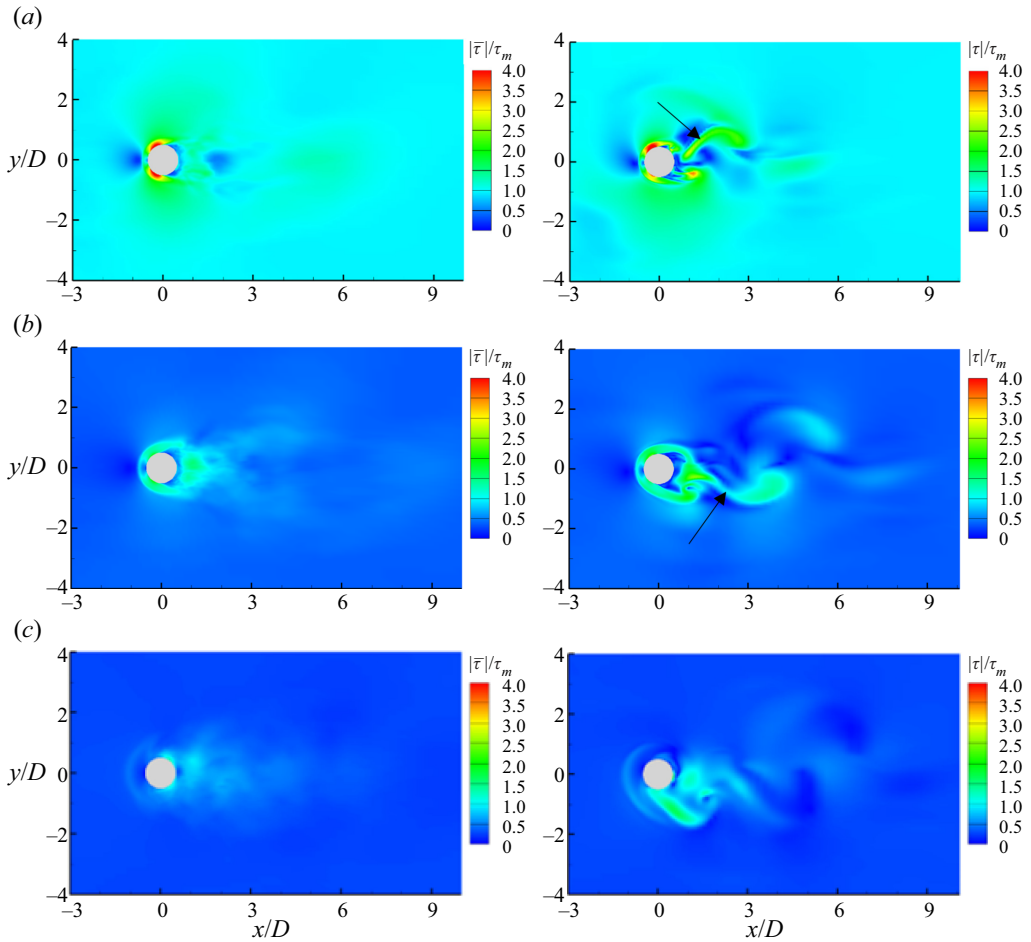


Figure 8. Non-dimensional bed shear stresses magnitude,  $|\bar{\tau}|/\tau_m$  and  $|\tau|/\tau_m$ , for the  $KC = 30.8$  test case (DES predictions): (a)  $t = T/4$  ( $\hat{u}' = 1$ ), (b)  $t = 3T/8$  ( $\hat{u}' = 0.7$ ); (c)  $t = T/2$  ( $\hat{u}' = 0$ ). The black arrows point towards regions of high  $|\tau|/\tau_m$  induced by horizontal near-bed vortices (see figure 5a).

stresses are relatively low at times when the incoming flow velocity magnitude is very low (see figure 8c for  $t = T/2$ ). However, regions of relatively high  $|\tau|/\tau_m$  are still generated in the instantaneous flow fields on the sides and at the back of the cylinder as the incoming velocity approaches zero. By contrast, the amplification of  $|\tau|/\tau_m$  at  $t = T/2$  (figure 8c) is negligible around the upstream face of the cylinder because the horseshoe vortex loses its coherence and moves away from the bed as the incoming flow velocity approaches zero.

For relatively low  $KC$  values, the core of the main horseshoe vortex increases considerably as the flow starts decelerating ( $t > T/4$ ). In the  $KC = 8$  case, the horseshoe vortex maintains its coherence past  $t = T/2$  when the incoming flow reverses and is able to induce relatively large bed shear stresses beneath it (e.g. see figures 5c and 9b for  $t = T/2$ ). On the wake side, the elongated streamwise-oriented horizontal vortex forming near  $y/D = 0$  and the near-bed vortex forming around the downstream face of the cylinder induce the largest bed shear stresses in the wake region at  $t = T/2$  (figure 9b). So, for oscillatory flow conditions, the bed shear stress distributions can be qualitatively very different from those observed for steady incoming flow especially at times when the

## Oscillatory flow around a vertical circular cylinder

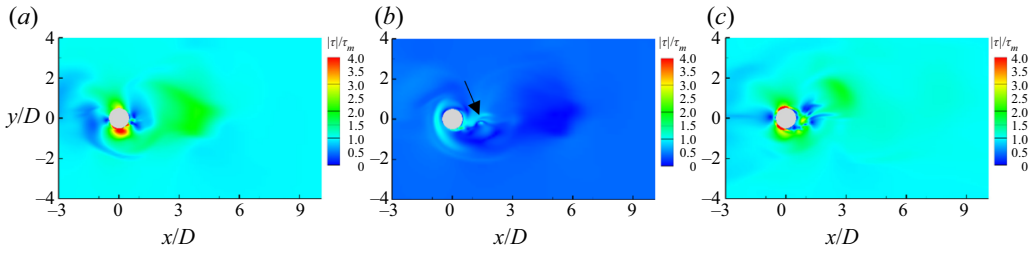


Figure 9. Non-dimensional bed shear stresses magnitude,  $|\tau|/\tau_m$  (DES predictions): (a)  $t = T/4$  for  $KC = 8$ ; (b)  $t = T/2$  for  $KC = 8$ ; (c)  $t = T/4$  for  $KC = 15.4$ . The black arrow in (b) points towards a region of high  $|\tau|/\tau_m$  induced by a horizontal near-bed vortex (see figure 5c for  $t = T/2$ ).

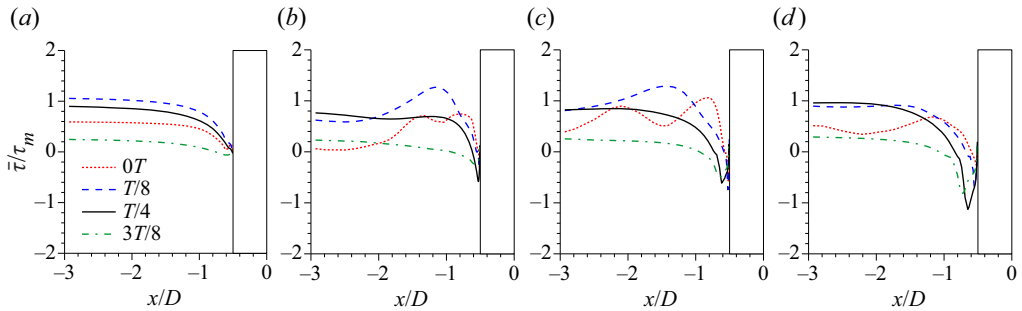


Figure 10. Non-dimensional phase-averaged bed shear stress,  $\bar{\tau}/\tau_m$ , in the symmetry ( $y/D = 0$ ) plane at the upstream ( $x/D < 0$ ) side of the cylinder (DES predictions): (a)  $KC = 1.5$ ; (b)  $KC = 8$ ; (c)  $KC = 15.4$ ; (d)  $KC = 30.8$ . The bed shear stress is plotted at  $t = 0T$  ( $\hat{u}' = 0$ ),  $t = T/8$  ( $\hat{u}' = 0.7$ ),  $t = T/4$  ( $\hat{u}' = 1$ ) and  $t = 3T/8$  ( $\hat{u}' = 0.7$ ).

velocity magnitude in the approaching flow is much lower than the peak approaching flow velocity.

### 4.3. Bed shear stresses and horseshoe vortex dynamics in the symmetry plane

Figure 10 compares the distributions of  $\bar{\tau}/\tau_m$  in the symmetry ( $y/D = 0$ ) plane at the upstream ( $x/D < 0$ ) side of the cylinder at relevant times during the oscillatory cycle. For  $KC \geq 8$ , a negative peak of  $\bar{\tau}$  is observed close to the cylinder when the incoming velocity magnitude is the highest ( $t = T/4$ ). This peak is induced by the horseshoe vortex. The magnitude of  $\bar{\tau}/\tau_m$  in this region increases with increasing  $KC$  to reach 1.2 for  $KC = 30.8$  (figure 10d). The negative peak is not present in the  $KC = 1.5$  case where no horseshoe vortex forms.

As opposed to the case of steady incoming flow where erosion on the upstream side of the cylinder, close to its symmetry line, is only driven by the horseshoe vortex, in the case of oscillatory flow erosion near the upstream face can also be induced by other mechanisms. This is the case for the  $KC = 8$  (figure 10b) and  $KC = 15.4$  (figure 10c) simulations where regions with  $|\bar{\tau}/\tau_m| > 1$  and  $|\tau/\tau_m| > 1$  form during the first half of the oscillatory cycle (e.g. see also figures 9a and 9c). The peak values of  $\bar{\tau}/\tau_m$  in figure 10 are close to 1.4 ( $t = T/8$ ,  $x/D \approx -1.2$ ) for  $KC = 8$  and 1.45 ( $t = T/8$ ,  $x/D \approx -1.6$ ) for  $KC = 15.4$ . The peak values beneath the horseshoe vortex are 0.6 ( $t = T/4$ ) for  $KC = 8$  and 0.8 ( $t = T/4$ ) for  $KC = 15.4$ . For these two cases, local scour on the upstream side of the cylinder is not primarily driven by the horseshoe vortices but rather by some of the wake vortices shed on

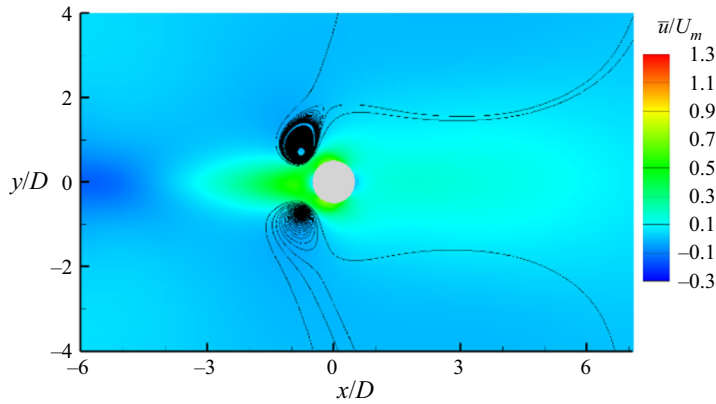


Figure 11. Phase-averaged streamwise velocity,  $\bar{u}/U_m$ , in a horizontal plane ( $z/H=1$ ) at  $t=0T$  ( $\hat{u}'=0$ ) in the  $KC=15.4$  simulation. The streamlines visualize the vortices that correspond to the two cells forming at the back of the cylinder ( $x/D > 0$ ) at earlier times when  $\hat{u}' < 0$ . The flow is accelerated towards the cylinder between the cores of these vortices once the two vortices move inside the  $x/D < 0$  region.

the downstream side of the cylinder that start moving towards the cylinder as the direction of the incoming flow changes during the next half of the oscillatory cycle (see discussion of figure 7). As these vortices pass the cylinder and move into the ‘upstream’ region, they accelerate some of the flow next to them which increases the bed shear stress. This is illustrated in figure 11 for the  $KC=15.4$  simulation. The two counter-rotating vortices in the  $x/D < 0$  region originated in the  $x/D > 0$  region during the previous half-period of the oscillatory cycle when  $\hat{u}' < 0$ . As they pass the cylinder, they generate between their cores a strong jet-like flow towards the cylinder. This effect is the strongest at times where the incoming velocity magnitude is small. As  $KC$  further increases, the wake vortices generally remain on the side of the cylinder where they were shed. This explains why a region with  $\bar{\tau}/\tau_m > 1$  is not present away from the cylinder in the  $KC=30.8$  simulation (figure 10d). It is only for such high- $KC$  cases that the horseshoe vortices are the main mechanism for scour on the upstream side of the cylinder.

On the downstream side of the cylinder, the variation of  $\bar{\tau}/\tau_m$  in the symmetry plane (figure 12) is qualitatively similar in the simulations conducted with  $KC \geq 8$ . As expected, the largest magnitudes are predicted at  $t=T/4$  when the incoming flow velocity magnitude is the largest. A first region of high values of  $|\bar{\tau}|/\tau_m$  is predicted inside the recirculation region at the back of the cylinder. It is mainly induced by the wake billows as they detach from the cylinder and start moving downstream (e.g. see VW vortices at  $t=T/4$  in figure 5a,b for  $KC=30.8$  and 15.4,  $|\bar{\tau}|/\tau_m$  distribution for  $KC=30.8$  in figure 8a and  $|\tau|/\tau_m$  distribution for  $KC=15.4$  in figure 9c). The shedding of the pair of counter-rotating vortices is more symmetric in the  $KC=8$  case (see VW vortices in figure 5c and  $\omega_z$  distribution in figure 7b). As a result, their capacity to accelerate the fluid towards the cylinder between their cores is also the largest, which explains why the peak negative value of  $\bar{\tau}/\tau_m$  in figure 12 is predicted for  $KC=8$ . The position of the peak negative bed shear stress moves away from the cylinder with increasing  $KC$ . A region of high positive values of  $\bar{\tau}/\tau_m$  is predicted in the near wake (e.g. see distribution of  $|\bar{\tau}|/\tau_m$  between  $x/D=3$  and  $x/D=8$  in figure 8a for  $KC=30.8$  and that of  $|\tau|/\tau_m$  between  $x/D=1.5$  and  $x/D=4$  in figure 9a for  $KC=8$ ) as the accelerated flow passing the cylinder moves towards the symmetry plane behind the flow recirculation region. Results in figure 12 show that the peak values inside this region decay monotonically with increasing  $KC$ , while the distance

## Oscillatory flow around a vertical circular cylinder

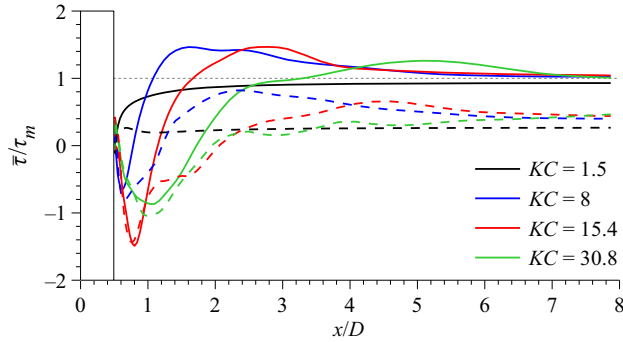


Figure 12. Non-dimensional phase-averaged bed shear stress,  $\bar{\tau}/\tau_m$ , in the symmetry ( $y/D=0$ ) plane at the downstream ( $x/D > 0$ ) side of the cylinder (DES predictions). Solid lines show results at  $t=T/4$  ( $\hat{u}' = 1$ ). Dashed lines show results at  $t=3T/8$  ( $\hat{u}' = 0.7$ ).

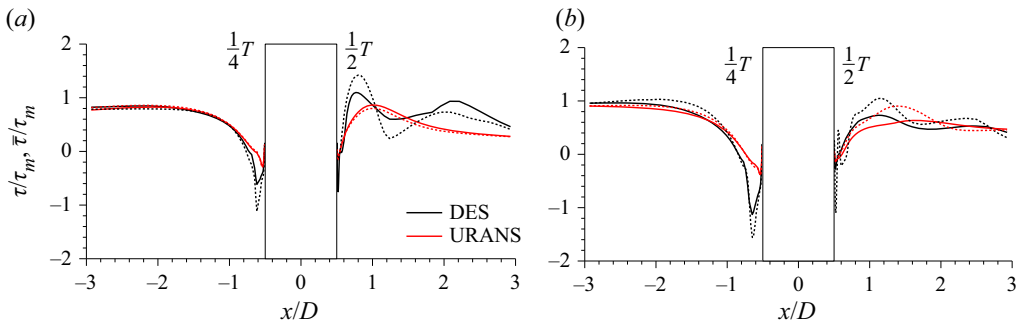


Figure 13. Non-dimensional instantaneous and phase-averaged bed shear stress,  $\tau/\tau_m$  and  $\bar{\tau}/\tau_m$ , along the  $x$  direction ( $y/D=0$  plane) at the upstream (horseshoe vortex) side of the cylinder at  $t=T/4$  ( $\hat{u}' = 1$ ) and at  $t=T/2$  ( $\hat{u}' = 0$ ): (a)  $KC = 15.4$ ; (b)  $KC = 30.8$ . Solid lines represent phase-averaged values. Dashed lines are used for instantaneous values during an oscillatory cycle when relatively large bed shear stress magnitudes are induced close to the cylinder.

from the cylinder where the peak value is reached increases from  $x/D = 1.5$  for  $KC = 8$  to  $x/D = 5.4$  for  $KC = 30.8$ . The streamwise distance over which the bed shear stress recovers towards the values in the incoming flow also increases with increasing  $KC$  (figure 12). For  $KC = 15.4$ , the peak values of  $|\bar{\tau}/\tau_m|$  inside the two regions are close to 1.45. However, in the  $KC = 8$  and 30.8 simulations, the magnitude of  $\bar{\tau}/\tau_m$  is larger inside the near-wake region than inside the recirculation region. For these cases, most of the scour on the downstream (wake) side will occur away from the cylinder if the bed is close to horizontal.

Figure 13 quantifies the variability of the bed shear stresses along the symmetry plane with respect to the phase-averaged values. During some of the oscillatory cycles the horseshoe vortex induces bed shear stresses that can be up to 50%–100% larger than the phase-averaged values. This level of amplification with respect to the phase-averaged values was also observed in the validation test case ( $KC = 20$ ). A high cycle-to-cycle variability of the bed shear stresses on the upstream side is also observed especially when the incoming flow velocity magnitude is small (e.g. at  $t=T/2$  in the  $x/D > 0$  region in figure 13a) and is mainly due to differences in the coherence/circulation of the wake vortices and their trajectories as they move on the other side of the cylinder (see discussion of figure 11). For both  $KC$  values, URANS simulations severely underpredict the peak

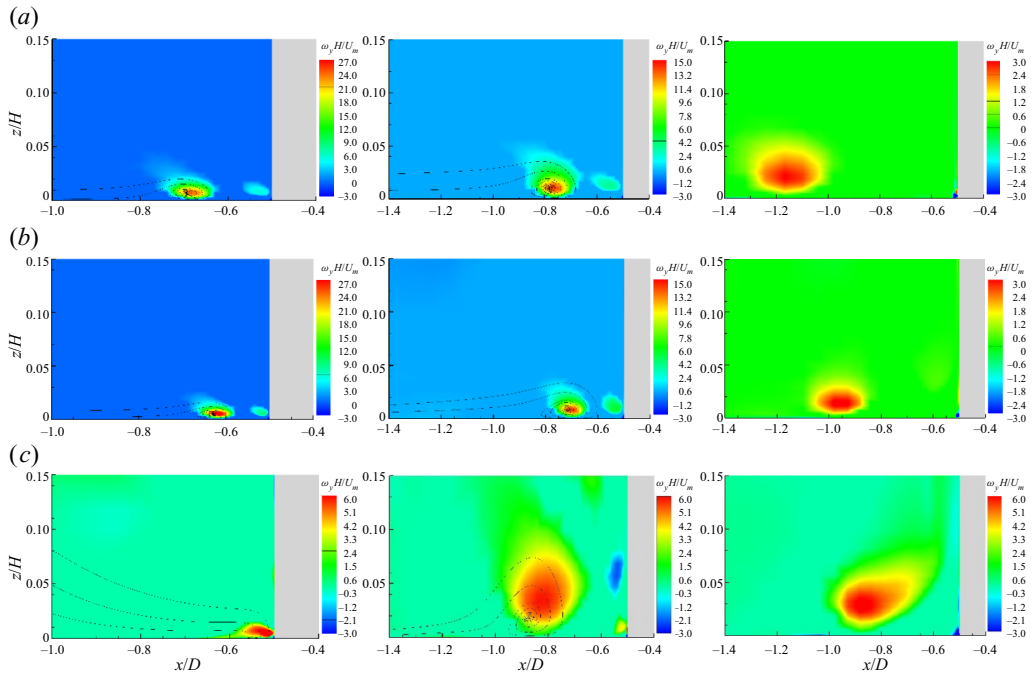


Figure 14. Non-dimensional out-of-plane vorticity,  $\omega_y H/U_m$ , at  $t = T/4$  ( $\hat{u}' = 1$ , left-hand panels),  $t = 3T/8$  ( $\hat{u}' = 0.7$ , middle panels) and  $t = T/2$  ( $\hat{u}' = 0$ , right-hand panels) during the oscillatory cycle in the  $y/D = 0$  plane visualizing the dynamics of the horseshoe vortices (DES predictions): (a)  $KC = 30.8$ ; (b)  $KC = 15.4$ ; (c)  $KC = 8$ .

magnitude of  $\bar{\tau}/\tau_m$  beneath the horseshoe vortex (e.g. by more than 100 % in the  $KC = 30.8$  case). The RANS simulation also underpredicts the peak values of  $\bar{\tau}/\tau_m$  induced by the advection of wake vortices on the upstream side of the cylinder (see predictions for  $t = T/2$  in figure 13a). The maximum bed shear stress predicted by RANS is  $\bar{\tau}/\tau_m = 1$  and the peak value is situated farther from the cylinder compared with DES. The differences between URANS and DES at  $t = T/2$  are much smaller in the  $KC = 30.8$  case.

Figure 14 provides more information of the dynamics of the main horseshoe vortex in the symmetry plane. This vortex forms a short time after the incoming flow velocity becomes positive. As  $KC$  decreases, the vortex forms closer to the cylinder. The patch of vorticity situated near the junction line between the cylinder and the bed in the  $KC = 15.4$  and  $30.8$  cases is not a horseshoe vortex. When the incoming flow velocity is the largest ( $t = T/4$ ), the circulation of the horseshoe increases monotonically with  $KC$ . This result is consistent with the bed shear stress distributions in figure 10 that show  $\bar{\tau}/\tau_m$  at  $t = T/4$  also increases with  $KC$  beneath the horseshoe vortex. As the flow decelerates ( $T/4 < t < T/2$ ), the main horseshoe vortex moves away from the cylinder in the  $KC = 30$  and  $15$  cases. This does not happen in the  $KC = 8$  case which is characterized by a large growth of the core of the horseshoe vortex between  $t = T/4$  and  $t = 3T/8$  (see also figure 5c) when the flow starts decelerating. In all simulations conducted with  $KC \geq 8$ , the horseshoe vortex survives past the time the incoming velocity reaches a zero value (e.g. it is still present in the flow fields at  $t = T/2$  in figure 5c) but completely loses its coherence shortly after the incoming flow changes direction. An increase in the size of the core during the deceleration phase ( $T/4 < t < T/2$ ) does not necessarily translate into an increase of the bed shear stress magnitude beneath the horseshoe vortex. This is because the increase in the size of the core

is generally accompanied by an increase of the distance between the axis of the vortex and the bed surface. Still, the large growth of the circulation in the  $KC = 8$  case between  $t = T/4$  and  $t = T/2$  is sufficient to generate a horseshow vortex with a relatively high capacity to entrain sediment near  $t = T/2$ , when the approaching flow velocity is zero (figure 9b).

### 5. Volumetric flux of entrained sediment

To characterize in an average way the capacity of the flow to entrain sediment, one has to consider not only the phase-averaged value of the bed shear stress,  $\bar{\tau}$ , but also the cycle-to-cycle variations of the instantaneous bed shear stresses with respect to the phase-averaged values. This is similar to the case of a cylinder with incoming steady flow; besides  $\bar{\tau}$  the values of the standard deviation of the bed shear stress should be considered when evaluating the capacity of the flow to entrain sediment (Sumer *et al.* 2003; Cheng *et al.* 2018). In the case where the incoming flow is oscillatory, some of the largest contributions to the instantaneous stress,  $\tau$ , are not due to random temporal variations of the coherence of some of the large-scale, near-bed coherent structures or of the paths followed by these eddies as they are advected away from the cylinder. Rather, the main reason for the very high amplification of the bed shear stress during some of the oscillatory cycles is the departure from the dominant wake-shedding pattern observed over most of the oscillatory cycles. A good example is the  $KC = 15$  case where sometimes two vortices are shed during a half-cycle instead of one vortex, which is the case for most of the half-cycles.

One simple way to assess the effect of varying the  $KC$  number on the sediment entrainment capacity of the flow around the cylinder at conditions corresponding to the start of the local scour process (e.g. flat bed) is to calculate the phase-averaged flux of entrained sediment based on the instantaneous flow fields,  $\bar{I}_n$ . Sediment entrainment formulas for non-cohesive sediment generally assume the sediment flux is proportional to  $(\tau - \tau_c)^\gamma$  with  $\gamma > 1$ , where  $\tau_c$  is the critical value for sediment entrainment for a given mean particle diameter,  $d_{50}$  (Chou & Fringer 2010). For example,  $\gamma = 1.5$  in van Rijn's (1984) formula to estimate the volumetric flux of sediment entrainment per unit time and area. This formula is often used in eddy-resolving simulations with a movable bed (e.g. see Chou & Fringer 2010). In non-dimensional form, the volumetric flux of sediment entrained from the bed at any given time during the oscillatory cycle with index  $n$  can be written as

$$I_n(t/T) = \frac{1}{\rho^{1.5} U_m^3 D^2} \int_{A'} (\tau - \tau_c)^{1.5} dA', \quad (5.1)$$

where  $A'(t)$  is the bed region of the whole computational domain where  $\tau(t, x, y) > \tau_c$  and  $0 < t/T \leq 1$ . The phase-averaged flux  $\bar{I}_n(t/T)$  is the average value of  $I_n$  over the  $N$  cycles used for phase averaging. Given that the series of simulations with varying  $KC$  were performed with constant  $H$ ,  $D$  and  $U_m$ , one can compare the erosive capability of the flow associated with local scour around the cylinder by assuming a constant value of  $\tau_c$  that is sufficiently large such that no erosion occurs in the undisturbed flow.

The sediment fluxes were calculated in figure 15 assuming  $\tau_c / \rho U_m^2 = 0.0048$ . This value was higher than the maximum bed shear stress away from the cylinder such that all entrainment is due to the presence of the cylinder. For example, assuming a laboratory-scale experiment performed with  $U_m = 0.18 \text{ m s}^{-1}$  and  $D = 0.04 \text{ m}$ , the aforementioned value of  $\tau_c$  will correspond to sediment with  $d_{50} = 0.3 \text{ mm}$  based on Shields' diagram. Relatively large differences are observed between  $\bar{I}_n$  and the values of the volumetric flux for some of the oscillatory cycles. Generally, this happens for the

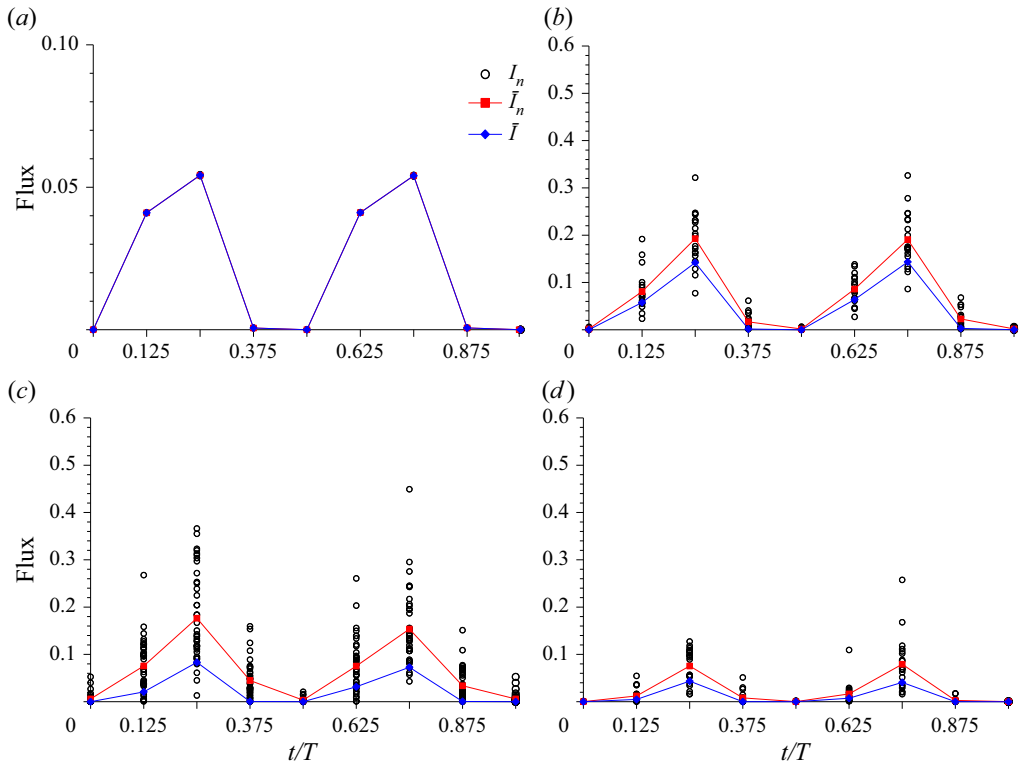


Figure 15. Non-dimensional volumetric flux of entrained sediment per unit time versus non-dimensional time,  $t/T$  (DES predictions): (a)  $KC = 1.5$ ; (b)  $KC = 8$ ; (c)  $KC = 15.4$ ; (d)  $KC = 30.8$ . Results are plotted for  $\tau_c/\rho U_m^2 = 0.0048$ . The symbols show the values of the instantaneous flux,  $I_n$ , for each oscillatory cycle ( $n = 1$  to 20) used to calculate the mean (phase-averaged) flux,  $\bar{I}_n$ . Also shown is the mean flux calculated using the phase-averaged bed shear stress,  $\bar{I}$ .

cycles in which the wake-shedding pattern and/or the coherence of the shed vortices are significantly different from those observed for most of the other oscillatory cycles. The combined effects of the cycle-to-cycle variations of the coherence of the main near-bed coherent structures and of the smaller-scale turbulent eddies on entrainment can be estimated by looking at the difference between  $\bar{I}_n$  and the entrainment flux calculated based on the phase-averaged bed shear stress,  $\bar{I} = (1/\rho^{1.5} U_m^3 D^2) \int_{A'} (\bar{\tau} - \tau_c)^{1.5} dA'$ . The values of  $\bar{I}$  are also included in figure 15.

For all  $KC$  values the fluxes  $\bar{I}_n$  and  $\bar{I}$  peak at  $t = T/4$  and  $3T/4$  when the velocity magnitude in the undisturbed flow is the largest. The largest cycle-to-cycle variation of  $I_n$  is observed for  $KC = 15.4$ . In this case, the maximum values of  $I_n/\bar{I}_n$  are larger than 2 over most of the cycle (figure 15c). This means that the volumetric flux of entrained sediment over some of the cycles can be much larger than the cycle-averaged value. Consistent with this result, the standard deviation of  $I_n$  is also the largest for the  $KC = 15.4$  case over most of the oscillatory cycle (figure 16). It is only when the undisturbed flow velocity is close to zero ( $t \approx 0T$  and  $T/2$ ) and the entrainment is negligible that the standard deviation of  $I_n$  is basically independent of  $KC$  (figure 16). The large variation of  $I_n$  in the  $KC = 15.4$  case is explained by the fact that this is the case with the most irregular wake-shedding pattern among the four cases analysed in figure 15.



## Oscillatory flow around a vertical circular cylinder

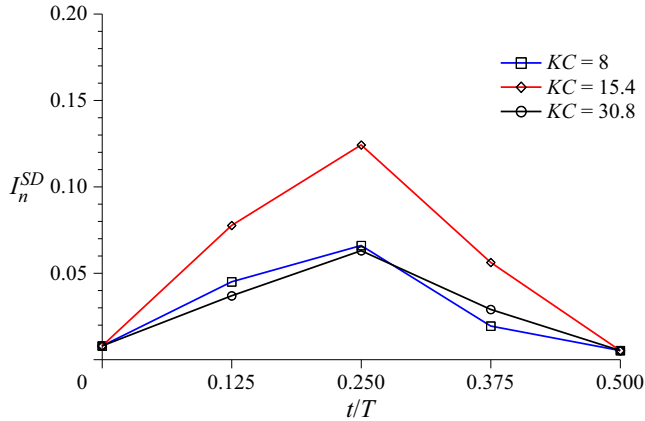


Figure 16. Standard deviation of the non-dimensional volumetric flux of entrained sediment per unit time versus non-dimensional time,  $t/T$  (DES predictions).

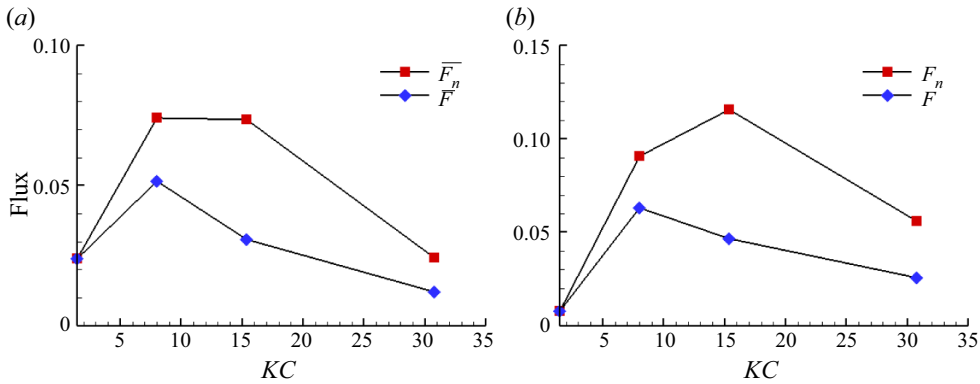


Figure 17. Mean non-dimensional volumetric flux of entrained sediment over one oscillatory cycle (DES predictions): (a)  $\tau_c/\rho U_m^2 = 0.0048$ ; (b)  $\tau_c/\tau_m = 1.5$ . The fluxes  $\bar{F}_n$  and  $\bar{F}$  are calculated based on  $I_n$  and  $\bar{I}$ , respectively.

The mean value of the volumetric flux of entrained sediment over one oscillatory cycle  $\bar{F}_n$  is obtained by integrating  $I_n$  from  $t/T = 0$  to  $t/T = 1$ . Similarly, one can calculate the volumetric flux of sediment entrained over one oscillatory cycle using the values of  $\bar{I}$  rather than  $I_n$ . This flux is denoted  $\bar{F}$ . Figure 17(a) shows that  $\bar{F}_n$  peaks for  $8 < KC < 15.4$  before starting to decrease for  $KC > 15.4$ . Meanwhile,  $\bar{F}$  peaks for  $KC \approx 8$  and then decreases monotonically with increasing  $KC$ . As expected,  $\bar{F} = \bar{F}_n$  for  $KC = 1.5$  as the flow is periodic. The ratio  $\bar{F}/\bar{F}_n$  decreases to 0.66 for  $KC = 8$  and is close to 0.5 for  $KC > 8$ . This means that coherent structures whose dynamics is not quasi-periodic (e.g. some of the shed wake vortices and near-bed vortices parallel to the bed) play a major role in sediment entrainment at relatively large  $KC$  numbers.

Another way to compare the sediment entrainment capacity of the flow among test cases with varying  $KC$  is to choose the values of  $H$ ,  $U_m$  and  $T$  such that the non-dimensional bed shear stresses induced in the undisturbed flow region are about the same, which means that  $\tau_m/\rho U_m^2$  should be independent of  $KC$ . In this case, the critical bed shear stress for sediment entrainment should be the same for all test cases. Figure 17(b) shows the

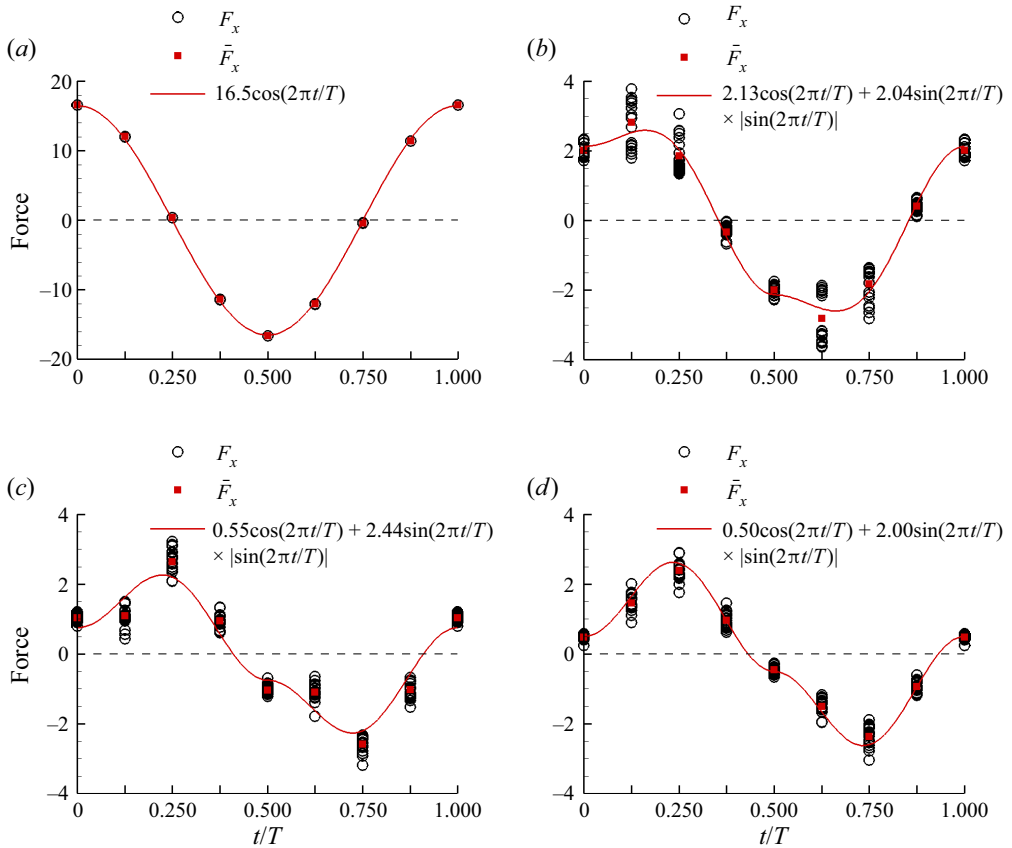


Figure 18. Non-dimensional (streamwise) in-line force versus non-dimensional time,  $t/T$  (DES predictions): (a)  $KC = 1.5$ ; (b)  $KC = 8$ ; (c)  $KC = 15.4$ ; (d)  $KC = 30.8$ . The open symbols show the values of the instantaneous in-line force,  $F_x$ , for each oscillatory cycle ( $n = 1$  to  $20$ ) used to calculate the mean (phase-averaged) drag force,  $\overline{F}_x$ . The instantaneous and phase-averaged values are very close for  $KC = 8$ . Also included (solid red line) is the in-line force  $\overline{F}_{IF}$  predicted using Morison's equation.

variations of  $\overline{F}$  and  $\overline{F}_n$  with  $KC$  assuming  $\tau_c/\tau_m = 1.5$ . Results in figures 17(a) and 17(b) are qualitatively similar. The only difference is that  $\overline{F}_n$  reaches its maximum for  $KC = 15.4$  when the flux is calculated assuming  $\tau_c/\tau_m = 1.5$ .

### 6. Forces acting on the cylinder

Figures 18 and 19 compare the non-dimensional phase-averaged streamwise and spanwise forces acting on the solid cylinder,  $\overline{F}_x(t/T)$  and  $\overline{F}_y(t/T)$ , for the test cases with unimodal forcing ( $1.5 \leq KC \leq 30.8$ ) based on DES predictions. Following the usual convention used for forces acting on obstacles in oscillatory unidirectional flow (e.g. see Williamson 1985), the total streamwise force will be referred to as the in-line force. The spanwise forces in the present geometrical set-up with a vertical cylinder correspond to the lift forces for cases where the cylinder is positioned horizontally (e.g. see Keulegan & Carpenter 1958). The instantaneous and phase-averaged forces were obtained by integrating the pressure and shear stresses over the surface of the cylinder, between the channel bottom and the top surface, and then normalizing by  $\rho U_a^2 DH$ , where  $U_a = 0.622 U_m$  is the mean value

Oscillatory flow around a vertical circular cylinder

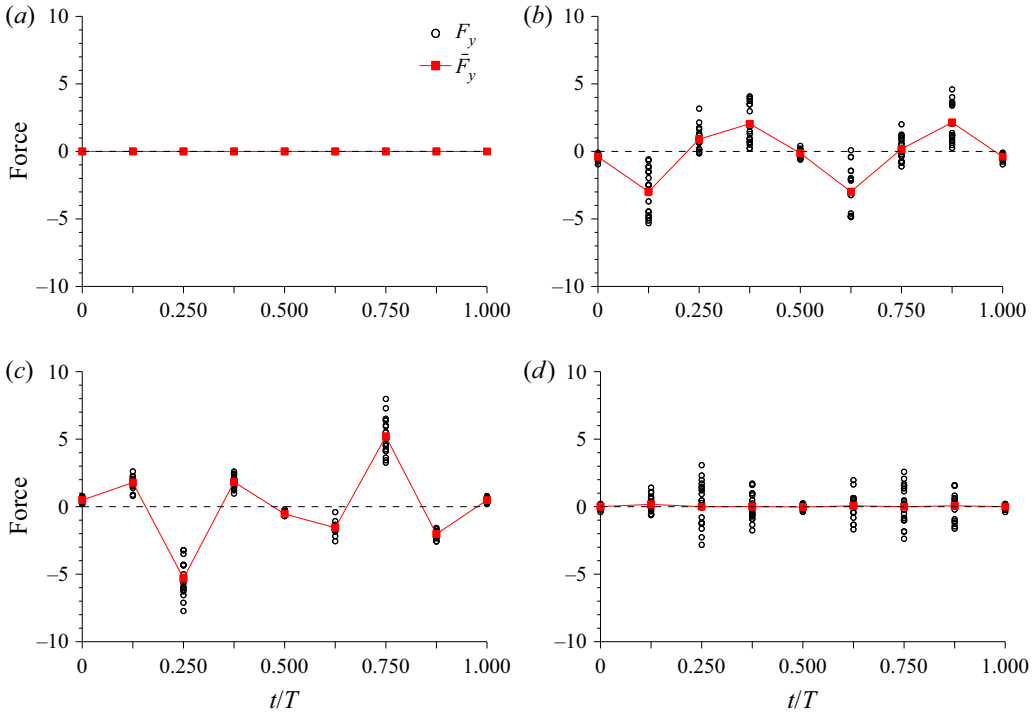


Figure 19. Non-dimensional spanwise force versus non-dimensional time,  $t/T$  (DES predictions): (a)  $KC = 1.5$ ; (b)  $KC = 8$ ; (c)  $KC = 15.4$ ; (d)  $KC = 30.8$ . The open symbols show the values of the instantaneous drag force,  $F_y$ , for each oscillatory cycle ( $n = 1$  to 20) used to calculate the mean (phase-averaged) force,  $\overline{F}_y$ .

of  $|\hat{u}|$  over one oscillatory cycle. The phase averaging was conducted over 20 oscillatory cycles. We checked that phase averaging over the first 10 cycles and over the last 10 cycles produced very similar results. Given the small height of the bottom boundary layer relative to the flow depth in the approaching flow (figure 2), no significant variations were observed in the distributions of the streamwise and spanwise forces per unit height when these forces were estimated over the whole height of the cylinder (figures 18 and 19) or only over the part situated outside of the bottom boundary layer.

For cylinders placed in oscillatory and wave flow, the prediction of the in-line force per unit length acting on the cylinder is modelled using an equation proposed by Morison *et al.* (1950) that splits the in-line force into two components due to the inertia and the drag force contributions. If the phase-averaged, in-line force non-dimensionalized by  $\rho U_a^2 D$  is denoted  $\overline{F}_{IF}(t/T)$ , then Morison's equation for a circular cylinder is

$$\overline{F}_{IF} = C_m \frac{\pi}{4} \frac{D}{TU_a^2} \frac{\partial \hat{u}}{\partial (t/T)} + C_d \frac{1}{2} \frac{\hat{u}|\hat{u}|}{U_a^2} = C_m \frac{\pi}{4} \frac{1}{0.622^2 KC} \frac{\partial \hat{u}'}{\partial (t/T)} + C_d \frac{1}{2} \frac{\hat{u}'|\hat{u}'|}{0.622^2}, \quad (6.1)$$

where  $C_m$  and  $C_d$  are the inertia and drag coefficients, respectively. Keulegan & Carpenter (1958) evaluated these coefficients based on experiments conducted with a horizontal cylinder placed below the free surface in a basin with standing waves surging in it. They found that for a circular cylinder  $C_m$  is close to 2.0 for small  $KC$  numbers and reaches a minimum ( $C_m \approx 0.7$ ) for  $KC \approx 15$ . It then starts to monotonically increase with  $KC$  to reach  $C_m \approx 2.5$  for  $KC = 120$ . For small  $KC$  numbers,  $C_d$  increases with  $KC$  to reach a value close to 2.3 for  $KC = 15$ . It then gradually decreases with increasing  $KC$  to reach

$KC = TU_m/D$	$C_m$	$C_d$	$F_{x,max}/(\rho U_m^2 DH)$	$C_{F_x}^{rms}$	$C_{F_y}^{rms}$	$\overline{F_x}^{rms}$	$M_x$
1.5	1.94	0	3.2	20.4	0.0	11.72	10.11
8.0	1.23	1.57	0.75	97.6	92.1	1.97	1.66
15.4	0.65	1.89	0.70	276.8	310.1	1.59	1.31
30.8	1.17	1.54	0.58	1044.6	83.6	1.50	1.24

Table 2. Non-dimensional variables characterizing the forces acting on the cylinder for the test cases conducted with purely oscillatory flow (one-mode forcing).

the steady flow value ( $C_d \approx 1.0$ ) for  $KC \gg 100$ . Using the expression for  $\hat{u}'$ , (6.1) can be written as

$$\overline{F_{IF}} = C_1 \cos\left(2\pi \frac{t}{T}\right) + C_2 \sin\left(2\pi \frac{t}{T}\right) \left| \sin\left(2\pi \frac{t}{T}\right) \right|. \quad (6.2)$$

Figure 18 shows the variation of  $\overline{F_x}$  together with a best-fit function for  $\overline{F_{IF}}$ . One can see that for all four cases  $\overline{F_{IF}}$  provides a fairly good approximation to  $\overline{F_x}$  over the oscillatory cycle. Using the  $C_1$  and  $C_2$  constants given in figure 18, one can calculate  $C_m$  and  $C_d$ . Despite the different set-up of the present simulations (e.g. orientation of the cylinder, Reynolds number) compared with that in the study conducted by Keulegan & Carpenter (1958), the predicted values of  $C_m$  and  $C_d$  (table 2) are fairly close to the values inferred from experiments (see figures 10 and 11 in Keulegan & Carpenter (1958)).

Table 2 also includes the values of the maximum magnitude of the in-line drag force  $F_{x,max}/(\rho U_m^2 DH)$  recorded over the oscillatory cycles analysed in figure 18. These forces are on average 15%–20% smaller than the values compiled by Keulegan & Carpenter (1958). The difference is partially due to the boundary layer forming at the channel bottom in the present simulations conducted with a vertical surface-mounted cylinder. The phase angles where the maximum force is reached are close to  $0^\circ$  and  $45^\circ$  in the  $KC = 1.5$  and 8 simulations, respectively. The phase angle is about  $90^\circ$  in the  $KC = 15.4$  and 30.8 simulations. If one accounts for the  $90^\circ$  phase difference in the forcing used in the experiments and present simulations, the values reported in figure 31 by Keulegan & Carpenter (1958) are similar to those predicted by the present simulations.

The variations of the in-line and spanwise forces during the oscillatory cycles can be used to calculate the root-mean-square (r.m.s.) of the two forces. Following Williamson (1985), the r.m.s. of the in-line and spanwise forces are reported in the form of a force coefficient where the force acting on the whole cylinder is non-dimensionalized by  $(\frac{1}{2}\rho(D^2/T^2)DH = \frac{1}{2}\rho(U_m^2/KC^2)DH)$ . The estimated values of the r.m.s. coefficients for the in-line ( $C_{F_x}^{rms}$ ) and spanwise ( $C_{F_y}^{rms}$ ) forces are also included in table 2. Williamson (1985) proposed an empirical formula,  $C_{F_x}^{rms} = (160KC^2 + 0.69KC^4)^{0.5}$ , that fitted very well the estimations of the r.m.s. of the in-line force based on his experimental data. The values given by this formula ( $C_{F_x}^{rms} = 19.0, 81.64, 277.0$  and  $879.1$  for  $KC = 1.5, 8.0, 15.4$  and  $30.8$ , respectively) are fairly close to the values estimated from the present simulations (table 2). The scatter in the experimental data (see figure 22 in Williamson (1985)) is very high for  $C_{F_y}^{rms}$  no and clear trend can be identified in the variation of  $C_{F_y}^{rms}$  with  $KC$  except for the fact that  $C_{F_y}^{rms}$  is expected to be very small for  $KC < 6$ . Most of the experiments predicted  $20 < C_{F_y}^{rms} < 100$  for  $KC > 6$  with a peak measured value close to 180 for  $KC \approx 11$ . The values reported in table 2 are consistent with this range except for  $KC = 15.4$  where  $C_{F_y}^{rms}$  is close to 310.0. This increase is attributed to the fact that, after

## Oscillatory flow around a vertical circular cylinder

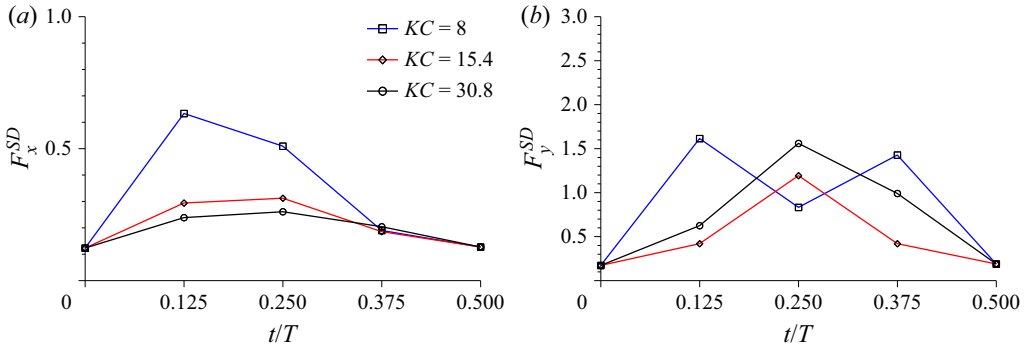


Figure 20. Standard deviation of the non-dimensional force acting on the cylinder along the streamwise and spanwise directions (DES predictions): (a)  $F_x^{SD}$ ; (b)  $F_y^{SD}$ .

formation on one side of the cylinder, most of the shed vortices are advected over the other side of the cylinder. Large spanwise forces are induced as these very coherent vortices move near one side of the cylinder. Moreover, this is also the case where the number of vortices shed over one half-cycle is not always the same.

For  $KC = 1.5$ ,  $\overline{F_x}$  is well approximated by a cosine function (figure 18a). This means that for sufficiently small  $KC$  numbers,  $\overline{F_x}(t)$  has the same (sinusoidal) shape as the velocity in the undisturbed flow but is out of phase with it (e.g.  $\overline{F_x}(t) \sim \hat{u}'(t + T/2)$ ). One should note that for this case  $C_d \approx 0$ , which confirms that for very small  $KC$  numbers the in-line force in unidirectional oscillatory flow is due only to inertia effects.

Once shedding occurs at the lee side of the cylinder ( $KC > 6$ ), the in-line force variation becomes more complex and the phase difference starts decreasing monotonically with increasing  $KC$  (figure 18b–d). The contributions of both the inertia force and the drag force components are significant in the simulations conducted with  $KC \geq 8$  (table 2). For  $KC = 30.8$ , the maximum and minimum values of the in-line force are close to in phase with the maximum and minimum velocities in the undisturbed flow occurring at  $t = T/4$  and  $t = 3T/4$ , respectively. Meanwhile,  $\overline{F_x}$  is small, but not equal to 0, at  $t = 0$  and  $T/2$  (figure 18d). The largest cycle-to-cycle variations of the instantaneous in-line force,  $F_x$ , are observed for  $KC = 8$ . This information is presented in a more quantitative way in figure 20(a) that shows the standard deviation of  $F_x$  with respect to the phase-averaged value at representative times during the oscillatory cycle. At lower  $KC$  numbers, the largest standard deviations of  $F_x$  occur during the time the incoming flow accelerates towards the cylinder (e.g.  $t \approx T/8$  for  $KC = 8$ ). Once the phase lag between  $F_x$  and  $\hat{u}'$  decreases, the largest standard deviations occur close to  $t = T/4$  ( $KC = 15.4$  and  $30.8$ ). The peak values of the standard deviation reduce by about 50% as  $KC$  increases from 8 to 15.4. Other relevant variables characterizing the ‘mean’ magnitude of the in-line forces experienced by the cylinder over the oscillatory cycle are the r.m.s. of  $\overline{F_x}$  and the momentum of the in-line force magnitude over the oscillatory cycle  $M_x = \frac{1}{2} \int_0^1 |\overline{F_x}| d(t/T)$ . Both  $\overline{F_x}^{rms}$  and  $M_x$  show a sharp decay as  $KC$  increases from 1.5 to 8. This is followed by a much milder monotonic decay regime for  $KC \geq 8$  (see figure 21 and table 2).

Figure 19 shows that for a range of  $KC$  numbers the cylinder is subject to significant phase-averaged spanwise forces during the oscillatory cycle. As expected, for cases with no shedding the mean and the instantaneous spanwise forces are equal to zero (e.g. see results for  $KC = 1.5$  in figure 19a). This is because the flow remains symmetric with respect to the  $y/D = 0$  axis. Interestingly,  $\overline{F_y}$  is also very close to zero during the oscillatory cycle

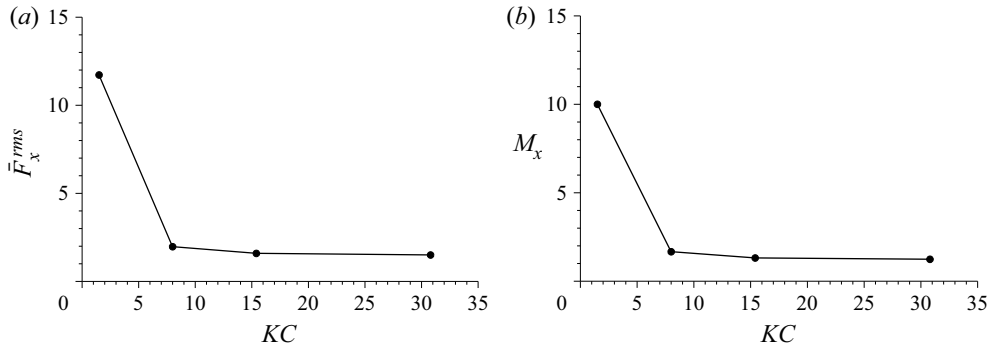


Figure 21. Oscillatory behaviour of the phase-averaged, non-dimensional (streamwise) in-line force,  $\overline{F_x}$  (DES predictions): (a) r.m.s. of  $\overline{F_x}$ ; (b) non-dimensional in-line force momentum over the half of the oscillatory cycle when  $\overline{F_x} > 0$ .

for sufficiently high  $KC$  numbers (e.g. see results for  $KC = 30.8$  in figure 19d). However, for large  $KC$  numbers, the cylinder can experience large instantaneous spanwise forces during some of the cycles. For example, the peak in-line forces occur at  $t = T/4$  and  $3T/4$  for  $KC = 30.8$ . At these times,  $|\overline{F_x}| \approx 2.5$  and the peak magnitude of  $F_x$  is close to 3. While for  $|\overline{F_y}| \approx 0$ , the peak magnitude of  $F_y$  is close to 3.5 at  $t = T/4$  and  $3T/4$ . These forces are mainly induced by some of the highly coherent vortices generated in the flow as they interact with the cylinder.

For  $KC = 8$  (figure 19b) and  $KC = 15.4$  (figure 19c), the oscillatory flow is characterized by non-zero mean spanwise forces. The peak magnitude of  $\overline{F_y}$  is close to 2.2 and 5.5, respectively. These values are significant given that the peak magnitudes of  $\overline{F_x}$  are close to 2.7 for both  $KC = 8$  and 15.5. The peak values of  $\overline{F_y}$  occur at times when also peak values are recorded for  $\overline{F_x}$ . This regime characterized by non-zero mean spanwise forces occurs for cases when at least one of the vortices shed during half of the oscillatory cycle moves back towards the cylinder and past it during the next half of the oscillatory cycle. In both cases, the peak magnitudes of  $F_y$  occur at times when the magnitude of  $\overline{F_y}$  is also high (e.g.  $t = T/8, T/4$  and  $3T/8$  for  $KC = 8$  and  $t = T/4$  for  $KC = 15.4$ ). This is confirmed by the variation of the standard deviation of  $F_y$  for these two cases shown in figure 20(b). As  $KC$  increases and the flow reaches a regime where the shed wake vortices do not move back past the cylinder, the standard deviation of  $F_y$  decays with increasing  $KC$  over most of the oscillatory cycle (e.g. compare results for  $KC = 15.4$  and 30.8 in figure 20b).

Figure 22 compares the phase-averaged in-line force coefficient for the cylinder,  $\overline{C_{Fx}} = \overline{F_x} / 0.5 \rho \hat{u}^2(t) DH$ , during the oscillatory cycle. Also shown are the in-line force coefficients,  $C_{Fx}$ , calculated using the instantaneous drag force,  $F_x$ , for each of the 20 oscillatory cycles used for phase averaging. These coefficients are similar to the standard streamwise drag coefficients defined in steady flow past cylinders. No values of  $C_{Fx}$  were included for the  $KC = 1.5$  case because the solution is periodic ( $\overline{C_{Fx}} = C_{Fx}$ ). The in-line force coefficient is not defined for  $t/T = 0$  and 0.5 when  $\hat{u} = 0$ . For  $KC > 15$ , the phase-averaged in-line force coefficients do not vary much the oscillatory cycle. This is different from cases with  $KC \leq 8$  for which the in-line force coefficient is equal to zero twice during the oscillatory cycle as the in-line force becomes zero for non-zero values of the incoming velocity. On average, the largest in-line force coefficients are predicted in the  $KC = 1.5$  case for which  $\overline{C_{Fx}} = 9-10$  except for times close to  $T/4$  and  $3T/4$  when the in-line force and the corresponding in-line force coefficient approach zero.

## Oscillatory flow around a vertical circular cylinder

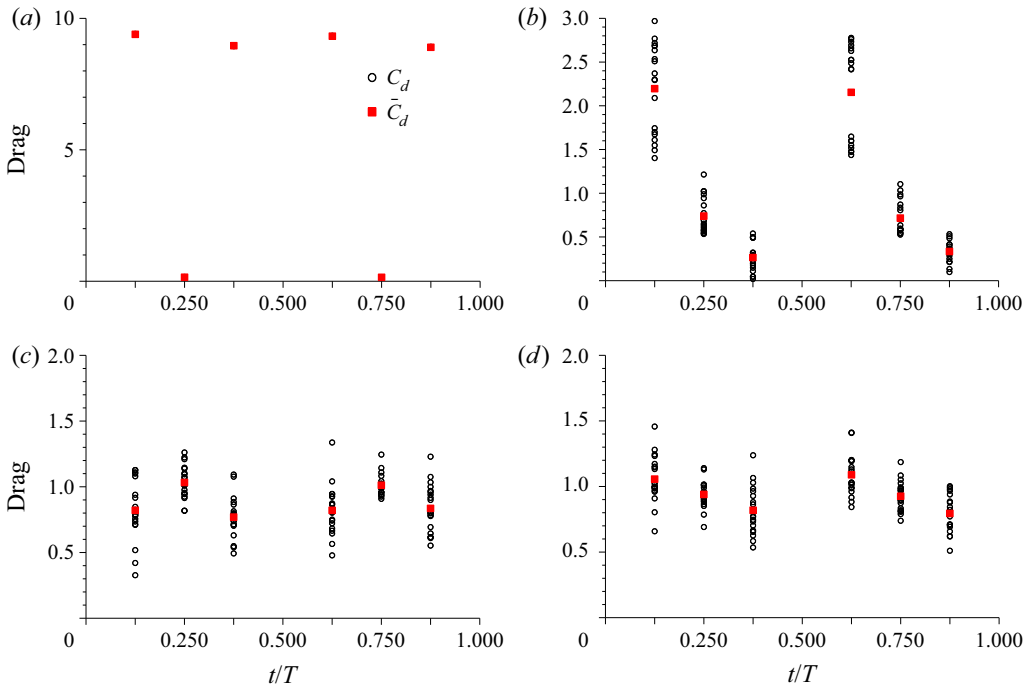


Figure 22. In-line force coefficient versus non-dimensional time,  $t/T$  (DES predictions): (a)  $KC = 1.5$ ; (b)  $KC = 8$ ; (c)  $KC = 15.4$ ; (d)  $KC = 30.8$ . The open symbols show the values of the instantaneous in-line force coefficient,  $C_{Fx}$ , for each oscillatory cycle ( $n = 1$  to  $20$ ) used to calculate the mean (phase-averaged) in-line force coefficient,  $\overline{C_{Fx}}$ . The instantaneous and phase-averaged values are very close for  $KC = 8$ . To get the force coefficient, the in-line force is non-dimensionalized with the depth-averaged streamwise velocity in the undisturbed flow,  $\hat{u}(t/T)$ , and the projected area,  $HD$ . No values can be calculated for  $t/T = 0$  and  $0.5$  when  $\hat{u} = 0$ .

It is also relevant to point out that  $\overline{C_{Fx}}$  varies roughly between 0.8 and 1.1 in the  $KC = 15.4$  and  $30.8$  cases with  $Re = 130\,000$ . A value of 1.2 is expected for the total drag coefficient of long cylinders in steady incoming flow with  $Re \approx 10^5$ . As the incoming velocity varies during the oscillatory cycle, the cylinder will experience lower physical Reynolds numbers. Still, the streamwise drag coefficient will not get below 0.9 as long as the Reynolds numbers remain larger than 2500, which will correspond to most of the oscillatory cycle in the cases discussed in this section. This result suggests that for sufficiently high  $KC$  numbers the phase-averaged in-line force coefficients during the oscillatory cycle are only 10%–15% smaller than the mean (time-averaged) drag coefficient for a case with incoming steady flow at the same Reynolds number. For circular cylinders, this result assumes that the physical Reynolds numbers defined with the unsteady undisturbed flow velocity are larger than 2500 and smaller than the Reynolds number at which the drag crisis starts.

As for the in-line force, the largest cycle-to-cycle variations in the values of  $C_{Fx}$  occur at  $t = T/8$  and  $5T/8$  in the  $KC = 8$  case (figure 22b). By contrast, the standard deviation of  $C_{Fx}$  varies much less during the oscillatory cycle in the  $KC = 15.4$  (figure 22c) and  $KC = 30.8$  (figure 22d) cases.

## 7. Summary and conclusions

The better performance of DES compared with URANS in predicting the maximum amplification of the bed shear stress in front and behind the surface-mounted vertical cylinder with incoming oscillatory flow was linked to the superior capability of DES to capture the formation, coherence and dynamics of the energetically important eddies in the flow. In agreement with previous numerical investigations of this type of flow (e.g. see Baykal *et al.* 2017), for sufficiently large  $KC$  numbers, DES predicted the formation and shedding of wake vortices whose cores remained close to vertical over the whole flow depth. This is different from the behaviour of these vortices in flow past a circular cylinder with steady incoming flow where the cores of these vortices become inclined and are severely stretched as they approach the bed surface (Kirkil & Constantinescu 2015). The fact that the cores remained close to vertical and were subject to minimal stretching as they interacted with the bed is the main reason why the largest instantaneous bed shear stresses beneath these vortices were comparable to the peak values recorded in the regions of strong flow acceleration near the cylinder. Wake vortices whose cores remain vertical as they reach the bed and that can induce large bed shear stresses can also occur with steady incoming flow but only for cylinders of non-circular shape that contain sharp corners (e.g. for rectangular cylinders, see Kirkil & Constantinescu 2009).

Besides the vertical wake vortices, DES predicted the formation of near-bed horizontal vortices at the back of the cylinder and inside the near-wake region. The formation mechanism of these vortices is driven by the interaction of the deformed cores of the vertical wake vortices with the bed surface. Similar to the finger (secondary) vortices forming in the wake of long cylinders due to the spanwise instabilities propagating along the cores of the main wake vortices, an eddy-resolving technique is needed to capture the formation of these near-bed vortices. The peak bed shear stresses occurred in the regions of strong flow acceleration forming close to the upstream face of the cylinder only at times when the incoming velocity magnitude was close to its peak values. At other times during the oscillatory cycle, the amplification of the bed shear stress was mainly driven by the cores of the wake billows, by the main horseshoe vortex and by some of the near-bed horizontal vortices.

The capability of DES to accurately predict the bed shear stress distributions around the cylinder for fixed bathymetry (e.g. flat bed) is particularly relevant for designing scour protection measures around pile foundations. Calibration of design formulas for the minimum size of the stone forming the rock apron around the pile requires estimation of the peak mean shear stress over the rock apron given a certain approach flow and pile geometry. Such an approach based on 3-D simulations was used by Wu, Zeng & Constantinescu (2021) for designing riprap apron protections at bridge abutments with a steady current. That approach can be easily used with a DES solver and extended for monopile foundations placed in oscillatory flow or for cases where the oscillatory flow is superimposed with a steady current.

Consistent with previous experimental and URANS studies of oscillatory flow past cylinders conducted at lower Reynolds numbers (e.g. Sumer *et al.* 1997; Baykal *et al.* 2017), the present high-Reynolds-number simulations with unimodal oscillatory flow showed that the wake structure, the number of vortices shed every half-cycle and the dynamics of these vortices are mainly dependent on the  $KC$  number. The predicted wake dynamics in the  $KC = 1.5$  case (no vortex shedding, periodic flow) and the  $KC = 15.4$  case (one vortex shed each half-period) is in good general agreement with the experimental observations of Sumer *et al.* (1997) for cases with  $KC < 23$ . The shedding of three vortices



in the  $KC = 30.8$  case is consistent with the increase of the number of shed vortices with increasing  $KC$  observed by Williamson (1985) and Sumer *et al.* (1997).

The present study showed that for  $KC$  numbers close to values where the number of shed vortices over each half-cycle increases by one (e.g.  $KC \approx 17$  where the number of shed vortices increases from one to two), the number of shed vortices is not always the same for all the half-cycles. For example, in the  $KC = 15.4$  simulation two vortices were sometimes shed over a half-cycle instead of one vortex. Such cases are characterized by the largest cycle-to-cycle variation of quantities of engineering interest like the phase-averaged variation of the flux of sediment entrained from the bed and the drag forces acting on the cylinder.

For  $KC$  numbers only slightly larger than the threshold value for the formation of wake vortices ( $KC \approx 6$ ), the dynamics of the wake vortices is quite different from that observed at large  $KC$  numbers where the anti-symmetric wake-shedding mode dominates, similar to the case of long cylinders. The  $KC = 8$  simulation revealed that two fairly symmetric vortices form at the back of the cylinder during each half-cycle. None of these vortices is advected into the wake during the half-cycle where they form. Rather these vortices move over the other side of the cylinder during the next half-cycle when the incoming flow reverses. Previous experimental studies also reported cases where some of the vortices shed at the back of the cylinder can be washed past the cylinder during the next half-cycle. The different wake dynamics observed for  $KC$  numbers for which two strongly coherent, counter-rotating vortices move past the cylinder during the next half-cycle was found to have important consequences in terms of the bed shear stress distributions near the cylinder. As the two vortices pass the cylinder, they induce a jet-like flow oriented towards the cylinder between their cores. This phenomenon happens at times when the incoming flow velocity magnitude is low and the peak velocity amplification is driven by these two vortices. The phase-averaged bed shear stress magnitudes generated during this part of the oscillatory cycle can be larger than those induced by the horseshoe vortex when its coherence is the highest during the oscillatory cycle. For such cases, the sediment erosion mechanisms close to the cylinder are much more complex than those observed for cylinders with steady incoming flow.

The availability of the 3-D instantaneous and phase-averaged velocity fields allowed estimating the variation of the sediment entrainment potential of the flow with the  $KC$  number. If the depth-averaged velocity in the undisturbed oscillatory flow was assumed constant, results showed that the mean (cycle-averaged) volumetric flux of sediment entrained from the bed over one oscillatory cycle peaks for  $8 < KC < 15.4$ . The volumetric flux of entrained sediment calculated using the phase-averaged flow field peaked for  $KC \approx 8$  and then decreased monotonically with increasing  $KC$ . This component was found to account for less than 50 % of the flux calculated based on the instantaneous flow fields for  $KC \geq 15.4$ . This means that coherent structures whose dynamics is not quasi-periodic (e.g. some of the shed wake vortices and near-bed vortices whose axes are parallel to the bed) play a major role in sediment entrainment at relatively large  $KC$  numbers.

In the  $KC = 1.5$  simulation the flow was periodic. The in-line force acting on the cylinder was unimodal but out of phase with the incoming velocity forcing. The spanwise force was equal to zero at all times. For sufficiently high  $KC$  numbers for vortices to form at the back of the cylinder, the phase-averaged in-line force variation became multimodal. Despite its simplifying assumptions, Morison's equation was found to approximate reasonably well the variation of the phase-averaged in-line force during the oscillatory cycle for a surface-mounted cylinder with  $1.5 \leq KC \leq 30.8$ . The inertia term was found to be the dominant one in the  $KC = 1.5$  simulation. The phase lag between the maximum values of

the incoming velocity magnitude and in-line force monotonically decayed with increasing  $KC$  such that the lag was close to zero for  $KC = 30.8$ . For  $KC \geq 15$ , the phase-averaged in-line force coefficients varied between 0.8 and 1.1 during most of the oscillatory cycle. The corresponding drag coefficient for a cylinder in steady flow at a Reynolds number defined with the peak incoming velocity is 1.2. This means that for sufficiently high  $KC$  numbers the phase-averaged in-line force coefficient during the oscillatory cycle is only 10%–15% smaller than the drag coefficient in steady flow past a cylinder at the same Reynolds number.

Quantification of the cycle-averaged and instantaneous forces acting on the cylinder revealed that, for a certain range of  $KC$  numbers, the phase-averaged and instantaneous spanwise forces were non-negligible. Over an intermediate range of  $KC$  numbers (e.g. for  $KC = 8$  and  $KC = 15.4$ ), the cylinder was subject to phase-averaged spanwise forces that were comparable to the peak phase-averaged in-line forces. At large  $KC$  numbers (e.g. for  $KC = 30.8$ ), the phase-averaged spanwise force was equal to zero over the whole oscillatory cycle but the cylinder was still subject to large instantaneous spanwise forces over part of the oscillatory cycle. These findings are relevant both for fatigue analysis and for applications where the cylinder is flexible (e.g. plant stems).

The present study provided detailed information on the flow physics and dynamics of coherent structures for the most canonical configuration (e.g. isolated, emerged circular cylinder). Using the knowledge acquired for this limiting case, one can analyse more complex cases of relevance to practical applications. They include cases in which the incoming flow has both an oscillatory component and a steady component, cases in which the cylinder is placed on a surface containing bedforms (Chang & Constantinescu 2013) and configurations containing an array of cylinders (e.g. offshore wind farms or circular patches of vegetation with a given porosity).

**Acknowledgements.** We would like to thank Professor M. Sumer for providing details of his experimental data and numerical simulations. We gratefully acknowledge the National Center for High-Performance Computing (NCHC) in Taiwan for providing the computational resources needed to conduct the simulations.

**Declaration of interests.** The authors report no conflict of interest.

#### Author ORCID*s*.

George Constantinescu <https://orcid.org/0000-0001-7060-8378>.

#### REFERENCES

- AKILLI, H. & ROCKWELL, D. 2002 Vortex formation from a cylinder in shallow water. *Phys. Fluids* **14** (9), 2957–2967.
- AN, H., CHENG, L. & ZHAO, M. 2015 Two-dimensional and three-dimensional simulations of oscillatory flow around a circular cylinder. *Ocean Engng* **109**, 270–286.
- APSILIDIS, N., DIPLAS, P., DANY, C. & BOURATSIS, P. 2015 Time-resolved flow dynamics and Reynolds number effects at a wall–cylinder junction. *J. Fluid Mech.* **776**, 475–511.
- BAYKAL, C., FUHRMAN, D., SUMER, B.M., JACOBSEN, N.G. & FREDSE, J. 2015 Numerical investigation of flow and scour around a vertical circular cylinder. *Phil. Trans. R. Soc. A* **373**, 2033.
- BAYKAL, C., SUMER, B.M., FUHRMAN, D., JACOBSEN, N.G. & FREDSE, J. 2017 Numerical simulation of scour and backfilling processes around a circular pile in waves. *Coast. Engng* **122**, 87–107.
- CHANG, K.S. & CONSTANTINESCU, G. 2013 Coherent structures in flow over two-dimensional dunes. *Water Resour. Res.* **49**, 2466–2460.
- CHANG, W.Y., CONSTANTINESCU, G., LIEN, H.G., TSAI, W.F., LAI, J.S. & LOH, C.H. 2013 Flow structure around bridge piers of varying geometrical complexity. *ASCE J. Hydraul. Engng* **139** (8), 812–826.
- CHANG, W.Y., CONSTANTINESCU, G. & TSAI, W.F. 2017 On the flow and coherent structures generated by an array of rigid energed cylinders place in an open channel with flat and deformed bed. *J. Fluid Mech.* **831**, 1–40.

## Oscillatory flow around a vertical circular cylinder

- CHANG, W.Y., CONSTANTINESCU, G. & TSAI, W.F. 2020 Effect of array submergence on flow and coherent structures through and around a circular array of rigid vertical cylinders. *Phys. Fluids* **32**, 035110.
- CHANG, W.Y., CONSTANTINESCU, G., TSAI, W.F. & LIEN, H.C. 2011 Coherent structures dynamics and sediment erosion mechanisms around an in-stream rectangular cylinder at low and moderate angles of attack. *Water Resour. Res.* **47** (12), W12532.
- CHENG, Z., KOKEN, M. & CONSTANTINESCU, G. 2018 Approximate methodology to account for effects of coherent structures on sediment entrainment in RANS simulations with a movable bed and applications to pier 1112 scour. *Adv. Water Resour.* **120**, 65–82.
- CHOU, Y.J. & FRINGER, O. 2010 A model for the simulation of coupled flow-bed form evolution in turbulent flows. *J. Geophys. Res.* **115**, C10041.
- DARGAHI, B. 1989 The turbulent flow field around a circular cylinder. *Exp. Fluids* **8**, 1–12.
- DUBIEF, Y. & DELCAYRE, F. 2000 On coherent-vortex identification in turbulence. *J. Turbul.* **1**, 1124.
- DUTSCH, H., DURST, F., BECKER, S. & LIENHART, H. 1998 Low-Reynolds-number flow around an oscillating circular cylinder at low Keulegan–Carpenter numbers. *J. Fluid Mech.* **360**, 249–271.
- ELSTON, J.R., BLACKBURN, H.M. & SHERIDAN, J. 2006 The primary and secondary instabilities of flow generated by an oscillating circular cylinder. *J. Fluid Mech.* **550**, 359–389.
- JUSTENSEN, P. 1991 A numerical study of oscillating flow around a circular cylinder. *J. Fluid Mech.* **222**, 157–196.
- KAMSANAM, W. 2014 Development of experimental techniques to investigate the heat transfer processes in oscillatory flows. PhD thesis, University of Leicester.
- KEULEGAN, G.H. & CARPENTER, L.H. 1958 Forces on cylinders and plates in oscillating fluid. *J. Res. Natl Bur. Stand.* **60** (5), 423–440.
- KEYLOCK, C.J., CONSTANTINESCU, S.G. & HARDY, R.J. 2012 The application of computational fluid dynamics to natural river channels: Eddy resolving versus mean flow approaches. *Geomorphology* **179**, 1–20.
- KIRKIL, G. & CONSTANTINESCU, G. 2009 Nature of flow and turbulence structure around an in-stream vertical plate in a shallow channel and the implications for sediment erosion. *Water Resour. Res.* **45**, W06412.
- KIRKIL, G. & CONSTANTINESCU, G. 2012 A numerical study of the laminar necklace vortex system and its effect on the wake for a circular cylinder. *Phys. Fluids* **24**, 073602.
- KIRKIL, G. & CONSTANTINESCU, G. 2015 Effects of cylinder Reynolds number on the turbulent horseshoe vortex system and near wake of a surface-mounted circular cylinder. *Phys. Fluids* **27**, 075102.
- KIRKIL, G., CONSTANTINESCU, G. & ETTEMA, R. 2009 DES investigation of turbulence and sediment transport at a circular pier with scour hole. *J. Hydraul. Engng ASCE* **135** (11), 888–901.
- KOKEN, M. & CONSTANTINESCU, G. 2011 Flow and turbulence structure around a spur dike in a channel with a large scour hole. *Water Resour. Res.* **47**, W12511.
- KOKEN, M. & CONSTANTINESCU, G. 2020 Flow structure inside and around a rectangular array of rigid, emerged cylinders located at the sidewall of an open channel. *J. Fluid Mech.* **910**, A2.
- LIU, Y., LI, S., YI, Q. & CHEN, D. 2016 Developments in semi-submersible floating foundations supporting wind turbines: a comprehensive review. *Renew. Sustainable Energy Rev.* **60**, 433–449.
- LOUWERSHEIMER, W.F., VERHAGEN, H.J. & OLTHOF, J. 2009 Scour around offshore wind turbine. In *Coastal Structures 2007* (ed. L. Franco, G.R. Tomasicchio & A. Lamberti), *Proceedings of the Fifth Coastal Structures International Conference, July, 2007, Venice, Italy*, pp. 1903–1912. World Scientific.
- MAHESH, K., CONSTANTINESCU, G. & MOIN, P. 2004 A numerical method for large eddy simulation in complex geometries. *J. Comput. Phys.* **197**, 215–240.
- MORISON, J.R., O'BRIEN, M.P., JOHNSON, J.W. & SCHAAF, S.A. 1950 The forces exerted by surface waves on piles. *J. Petrol. Tech. Am. Inst. Mining Energy* **189**, 149–164.
- NEHARI, D. & BALLIO, F. 2004 Three-dimensional analysis of the unidirectional oscillatory flow around a circular cylinder at low Keulegan–Carpenter and  $\beta$  numbers. *J. Fluid Mech.* **520**, 157–186.
- OBASAJU, E.D., BEARMAN, P.W. & GRAHAM, J.M.R. 1988 A study of forces, circulation and patterns around a circular cylinder in oscillating flow. *J. Fluid Mech.* **196**, 467.
- PETERSEN, T.U., SUMER, B.M., FREDSDØE, J., FUHRMAN, D.R. & CHRISTENSEN, E.D. 2014 *Scour around Offshore Wind Turbine Foundations*. Technical University of Denmark. Department of Mechanical Engineering.
- RHIE, C.M. & CHOW, W.L. 1983 Numerical study of the turbulent flow past an airfoil with trailing edge separation. *AIAA J.* **21** (11), 1525–1532.
- VAN RIJN, L.C. 1984 Sediment pick-up functions. *J. Hydraul. Engng ASCE* **110** (10), 1494–1503.
- RODI, W., CONSTANTINESCU, G. & STOEISSER, T. 2013 *Large Eddy Simulation in Hydraulics*. CRC, Taylor & Francis Group.

- ROULUND, A., SUMER, B.M., FREDSE, J. & MICHELSEN, J. 2005 Numerical and experimental investigation of flow and scour around a circular pile. *J. Fluid Mech.* **534**, 351–401.
- SARPKAYA, T. & ISSACSON, M. 1981 *Mechanics of Wave Forces on Offshore Structures*. Van Nostrand Reinhold.
- SIMPSON, R.L. 2001 Junction flows. *Annu. Rev. Fluid Mech.* **33**, 415–443.
- SPALART, P. 2009 Detached eddy simulation. *Annu. Rev. Fluid Mech.* **41**, 181–202.
- STAHLMANN, A. 2014 Numerical and experimental modelling of scour at foundation structures for offshore wind turbines. *J. Ocean Wind Energy* **1**, 82–89.
- STRELETS, M. 2001 Detached Eddy simulation of massively separated flows. *AIAA* 2001-0879.
- SUMER, B.M., CHRISTIANSEN, N. & FREDSE, J. 1997 The horseshoe vortex and vortex shedding around a vertical wall-mounted cylinder exposed to waves. *J. Fluid Mech.* **332**, 41–70.
- SUMER, B.M., CHUA, L.H., CHENG, N.S. & FREDSE, J. 2003 Influence of turbulence on bed load sediment transport. *J. Hydraul. Engng ASCE* **129** (8), 585–596.
- SUMER, B.M. & FREDSE, J. 1997 *Hydrodynamics around Cylindrical Structures*. World Scientific.
- TATSUNO, M. & BEARMAN, P.W. 1990 A visual study of the flow around an oscillating circular cylinder at low Keulegan–Carpenter numbers and low Stokes numbers. *J. Fluid Mech.* **211**, 157–182.
- TONG, F., CHENG, L., XIONG, C., DRAPER, S., AN, H. & LOU, X. 2017 Flow regimes for a square cross-section cylinder in oscillatory flow. *J. Fluid Mech.* **813**, 85–109.
- TRAVIN, A., SHUR, M., STRELETS, M. & SPALART, P.R. 2000 Detached-eddy simulations past a circular cylinder. *Flow Turbul. Combust.* **63**, 293–313.
- WILCOX, D.C. 2006 *Turbulence Modeling in CFD*, 3rd edn. DCW Industries.
- WILLIAMSON, C.H.K. 1985 Sinusoidal flow relative to circular cylinders. *J. Fluid Mech.* **155**, 141–174.
- WU, H., ZENG, J. & CONSTANTINESCU, G. 2021 A multiparameter design formula for riprap size selection at wing-wall abutments. *J. Hydraul. Res.* **59** (4), 651–661.
- YANG, Y. & ROCKWELL, D. 2002 Wave interaction with a vertical cylinder: spanwise flow patterns and loading. *J. Fluid Mech.* **460**, 93–118.
- ZANG, Y., TANG, C. & NEPF, H. 2017 Turbulent kinetic energy in submerged model canopies under oscillatory flow. *Water Resour. Res.* **54**, 1734–1750.
- ZENG, J. & CONSTANTINESCU, G. 2017 Flow and coherent structures around circular cylinders in shallow water. *Phys. Fluids* **29** (6), 066601.
- ZENG, J., CONSTANTINESCU, S.G. & WEBER, L. 2008 A 3D non-hydrostatic model to predict flow and sediment transport in loose-bed channel bends. *IAHR J. Hydraul. Res.* **46** (3), 356–372.
- ZHAO, M. & CHENG, L. 2014 Two-dimensional numerical study of vortex shedding regimes of oscillatory flow past two circular cylinders in side-by-side and tandem arrangements at low Reynolds numbers. *J. Fluid Mech.* **751**, 1–37.